Bio-inspired autonomous visual vertical control of a quadrotor UAV

Article

Accepted Version

Central Archive at the University of Reading

Reading's research outputs online

Bio-inspired Autonomous Visual Vertical Control of A Quadrotor UAV

Mohamad T. Alkowatly Victor M. Becerra and William Holderbaum.

University of Reading, Reading, RG6 6AX, UK

Abstract

Near ground maneuvers, such as hover, approach and landing, are key elements of autonomy in unmanned aerial vehicles. Such maneuvers have been tackled conventionally by measuring or estimating the velocity and the height above the ground often using ultrasonic or laser range finders. Near ground maneuvers are naturally mastered by flying birds and insects as objects below may be of interest for food or shelter. These animals perform such maneuvers efficiently using only the available vision and vestibular sensory information. In this paper, the time-to-contact (Tau) theory, which conceptualizes the visual strategy with which many species are believed to approach objects, is presented as a solution for Unmanned Aerial Vehicles (UAV) relative ground distance control. The paper shows how such an approach can be visually guided without knowledge of height and velocity relative to the ground. A control scheme that implements the Tau strategy is developed employing only visual information from a monocular camera and an inertial measurement unit. To achieve reliable visual information at a high rate, a novel filtering system is proposed to complement the control system. The proposed system is implemented on-board an experimental quadrotor UAV and shown not only to successfully land and approach ground, but also to enable the user to choose the dynamic characteristics of the approach. The methods presented in this paper are applicable to both aerial and space autonomous vehicles.

PhD student, School of Systems Engineering, `m.t.alkowatly@pgr.reading.ac.uk`
Professor of Automatic Control, School of Systems Engineering, Senior Member AIAA, `v.m.becerra@reading.ac.uk`
Senior Lecturer, School of Systems Engineering, `w.holderbaum@reading.ac.uk`

Nomenclature

a_x, a_y, a_z	=	body accelerations in body axes frame (m/s)
d	=	rotor drag factor (dimensionless)
$\boldsymbol{F}^b$	=	total force acting on the quadrotor in body frame (N)
f	=	camera focal length (m)
g	=	acceleration due to gravity (m/s^2)
I_{xx}, I_{yy}, I_{zz}	=	moments of inertia about body axes (kg m^2)
J	=	rotor inertia (rad/s)
ℓ	=	quadrotor arm length (m)
m	=	quadrotor mass (kg)
n	=	rotor lift factor (dimensionless)
p, q, r	=	body angular rates about roll, pitch, and yaw body axes (rad/s)
Q_i	=	drag torque of propeller i (N m)
T_a	=	total quadrotor thrust force (N)
$\mathbb{T}_c$	=	time-to-contact (s)
T_i	=	lift force of propeller i (N)
t_{nef}	=	normalized effective execution time
t_{ef}	=	effective execution time (s)
u, v	=	optic flow components in the image horizontal and vertical directions (pixel/s)
v_x, v_y, v_z	=	body translational velocities in body axes (m/s)
v_x^c, v_y^c, v_z^c	=	camera transnational velocities in camera axes (m/s)
$\boldsymbol{V}^b$	=	body frame translational velocity vector (m/s)
p^c, q^c, r^c	=	camera angular velocities in camera axes (rad/s)
z	=	vertical height (m)
z_{nef}	=	normalized effective final height (m)
ϕ, θ, ψ	=	roll, pitch, and yaw body attitude angles (rad)
τ	=	Tau optical variable (s)
$\boldsymbol{\tau}^b$	=	total torque acting on the quadrotor in body frame (N m)
$\boldsymbol{\tau}_x, \boldsymbol{\tau}_y$	=	control induced torques (N m)
$\boldsymbol{\tau}_z$	=	drag induced torque (N m)
$\boldsymbol{\tau}_J$	=	gyroscopic torque (N m)
Ω_h	=	rotor angular velocity in hover (rad/s)
Ω_i	=	rotor angular velocity of motor i (rad/s)
Ω_{res}	=	residual rotor angular velocity (rad/s)
$\omega_{b/e}^e$	=	angular velocity of body frame wrt earth frame expressed in earth frame(rad/s)
$\omega_{b/e}^b$	=	angular velocity of body frame wrt earth frame expressed in body frame(rad/s)
ω_x, ω_y	=	ventral flow in the x and y body directions (pixel/s)
ω_z	=	image dilation (pixel/s)
ω_x^c, ω_y^c	=	ventral flow in the x and y image directions (pixel/s)

Subscripts

0	=	initial
e	=	effective
f	=	final
n	=	normalized
r	=	reference

I. Introduction

Operating unmanned flying vehicles is useful yet challenging when the vehicle interacts with the environment. This interaction could be in the form of landing on ground or landing pads, docking into a station, or approaching terrain for inspection. Such tasks are easily solved when the vehicle is remotely piloted, especially when the pilot has a first person view of the environment, however this might not always be possible due to the unavailability of a suitable data link (for instance, when communications have been jammed) or when there are long delays on the data link, as in the case of space vehicles. Thus, it is important to find effective and flexible strategies to enable vehicles to perform such tasks autonomously.

To address this challenge, various researchers have used a combination of vision and range finder sensors in different configurations. In one configuration, the vision sensor has been mostly used for lateral stabilization or alignment with the landing site while the range finder is used for vertical control [1], [2]. In another configuration, the vision information is used to aid the state estimation needed for a conventional control strategy to achieve tasks

such as landing [3], [4], [5], [6], [7], [8] or even autonomous air refueling [9]. The problem with using range finder sensors is the trade off between weight, power consumption and resolution. Vision sensors, on the other hand, are cheap, lightweight and can provide high resolution, however using them conventionally to aid inertial navigation requires additional computation to resolve the visual information into an external inertial reference frame.

Birds and insects, on the other hand, solve navigation problems in simple and efficient ways. Bees achieve navigation tasks, such as negotiating narrow gaps and landing, simply by maintaining the observed retinal flow constant at a specific value [10]. This constant optic flow strategy not only alleviates the need to resolve the image based information in an inertial frame, but provides a control strategy to achieve the task in question as well. A constant optic flow strategy has been implemented on an aerial vehicle [11] and simulated on a moon lander vehicle [12] for achieving autonomous landing. However, both implementations require an external pitch control policy to achieve the landing task. A modified version of constant optic flow strategy has been implemented on a quadrotor UAV to achieve visual autonomous vertical landing by keeping image dilation constant using a closed loop control strategy [13].

All the aforementioned bio-inspired systems achieve autonomous landing visually without relying on range sensors. Reliable range sensors are either very expensive (such as LIght Detection And Ranging (LIDAR) sensors) or limited in operating distance (for example, ultrasonic sensors) [14]. On the other hand, vision sensors are small-sized, lightweight, and can operate over longer distances compared with ultrasound sensors, and are cheaper than LIDAR sensors. Vision sensors can also provide rich and high rate information using low power if the optic flow estimation is offloaded onto specialized chips [15], [16]. In addition, vision sensors are passive, allowing for stealth operation as opposed to range sensors.

One main drawback of constant optic flow and constant image dilation strategies is that these approaches are limited to asymptotic landing, which does not allow shaping of the maneuver's dynamics or the ability to perform other vertical maneuvers. In 1976, Lee proposed a visual guidance strategy to approach objects using the image based visual variable (Tau) that reflects the instantaneous time to contact [17]. This variable has been used to initiate actions such as car braking when approaching obstacles [17], [18]. Tau has been used for the initiation of wings folding of gannets before diving safely into the sea [19]. In addition, controlling Tau allows changing the dynamics of approach [20], it enables pigeons to adjust the final state of the approach when landing [21], and it gives hummingbirds the ability to perform aerial docking into flowers [22].

Although the value of the time to contact has been used previously in autonomous aerial navigation [23], [24], the first preliminary simulation results of using Tau as a visual control strategy to achieve fully autonomous landing are given in [25]. Those results have been obtained under the assumption of perfect knowledge of visual variables and neglecting the effects of the control system dynamics. Simulation results of a Tau theory inspired guidance law to achieve landing and perching of a UAV with an articulated leg is illustrated in [26] which is achieved via tracking an attitude and position trajectory generated using Tau theory. Similarly, in recent work [27] the author has demonstrated the application of Tau theory as a guidance law to achieve time and space controlled landing and docking maneuvers of UAVs. The proposed system has been validated experimentally on a synthetic Tau signal estimated from IMU measurements. None of these works have implemented Tau theory in a vision-in-the-loop fashion; nonetheless, they highlight the relevance and applicability of Tau theory to achieve autonomous range-free vertical control of aerial robots.

As visual information is inherently noisy, it is common in autonomous robotics to fuse this information with values originating from Inertial Measurement Units (IMU). While the vestibular system (or the IMU in robotics) provides information about angular rates and linear accelerations in the body frame, the visual information is presented in the eye (or camera) frame. Many researchers have presented different solutions to fuse the IMU and visual information to achieve better estimation of kinematic variables in an inertial frame [28], [8], [29]. However, as in this research, when the variables are controlled directly in the image frame then it is more appropriate to fuse information such that the IMU measurements are used to improve the estimates of the visual variables.

In this paper, a control strategy based on Tau theory is investigated and experimentally tested, showing its application in autonomous near ground maneuvers, in addition to its utility to influence the dynamics of the maneuver in each case. The term "near ground maneuvers" is used to refer to a set of maneuvers involving control of relative distance to the ground. The word *near* is interpreted in a visual context where an object is said to be near if it is visually perceivable by the vision system. The emphasis of the paper is on presenting the biologically inspired visual guidance strategy which is fulfilled via the high-level control system and the visual parameters estimation filter proposed in this paper. The proposed guidance system in turn uses a low-level stabilizing tracking control to achieve a flexible autonomous visual vertical control strategy for a quadrotor UAV.

The contribution of this paper is twofold. Firstly, a novel visual bio-inspired autonomous vertical control system is proposed and implemented onboard a quadrotor UAV to achieve autonomous landing and ground approach. Secondly, a novel IMU-aided visual motion parameters filter is proposed and implemented, which increases the

reliability and rate of the controlled visual parameters, allowing tighter control.

The paper is organized as follows: The basics of Tau theory and its applications to UAV vertical control are presented in section II; the body-centric quadrotor model is presented in section III; the proposed control architecture is demonstrated in section IV; the visual parameters registration and filtering scheme is presented in section V; the experimental framework and results are given in section VI; section VII analyzes the experimental results and gives comparisons with the theoretical results, and section VIII concludes the paper.

II. BASICS OF TAU THEORY

In a Cartesian coordinated frame attached to a subject, if an object is at a distance $z > 0$ along some axis (the z-axis for instance) pointing towards the object from a subject, then the time-to-contact with the object is defined as $T_c = -\frac{z}{\dot{z}}$. This value is the reciprocal of image dilation [17], hence it can be registered visually without knowledge of the distance or the velocity. Tau is an associated visual variable defined as follows:

$$\tau = \frac{z}{\dot{z}} \tag{1}$$

which is only defined when the subject is in relative motion with the object on the z-axis.

Closing a gap (approaching ground in the case of this paper) using a Tau strategy can be achieved by holding $\dot{\tau}$ constant at some value k during the maneuver. Contrary to the constant dilation strategy, with the Tau strategy one has the ability to control the dynamics of the gap closure with a suitable choice of the maneuver constant k. Taking the time derivative of (1) gives:

$$\dot{\tau} = 1 - \frac{z\ddot{z}}{\dot{z}^2} \tag{2}$$

If the rate of change of Tau is held constant during the maneuver, $\dot{\tau} = k$, the equation of motion describing the position of the object z, and its time derivatives (the relative object vertical velocity v and acceleration a) are found from the solution of the nonlinear first order differential equation (2):

$$
\begin{aligned}
z &= z_0 \left(1 + \frac{kt}{\tau_0} \right)^{(1/k)} \\
v &= v_0 \left(1 + \frac{kt}{\tau_0} \right)^{(1/k)-1} \\
a &= \frac{v_0^2}{z_0}(1-k) \left(1 + \frac{kt}{\tau_0} \right)^{(1/k)-2}
\end{aligned}
\tag{3}
$$

where $\tau_0 = \frac{z_0}{v_0}$ is the initial value of Tau given by the ratio of the initial height z_0 to the initial vertical velocity v_0 at the start of the maneuver.

To visualize the effect of the choice of k independently from the initial conditions, position, velocity and acceleration, each of the equations in (3) are normalized by z_0, v_0, and $\frac{v_0^2}{z_0}(1-k)$, respectively. Time is normalized by the theoretical time value at which the maneuver ends. This value can be found from (3) by setting $z = 0$ and is equal to $\frac{-\tau_0}{k}$. Normalized object position z_n, relative velocity v_n and acceleration a_n are plotted against normalized time for different values of k, as shown in Figure 1.

A simple analysis of the equations of motion (3) and the cases visualized in Figure 1 shows that the choice of k can result broadly in one of the following profiles:

1) $k > 1$ results in an uncontrolled collision. The gap will close with non-zero forward velocity and acceleration at closure.
2) $k = 1$ results in an uncontrolled collision. Zero acceleration is applied hence the gap will close with the initial constant velocity.
3) $0.5 < k < 1$ results in a gap closure with increasingly applied deceleration which theoretically terminates with zero velocity at contact. However, the demanded accelerations at the end of the maneuver tend to be high, and are thus likely to cause control saturation. As a result, this case is likely to close the gap with hard contact having a non-zero velocity residual. The closure is characterized by a delayed high deceleration.
4) $k = 0.5$ results in a gap closure with soft contact, involving a constantly applied deceleration which terminates with zero velocity at contact.
5) $0 < k < 0.5$ results in a gap closure with a soft contact, involving a decreasingly applied deceleration which terminates with zero velocity at contact. The closure is characterized by an early sharp deceleration.

There are two additional choices of k not normally covered in the literature on Tau theory, and not shown in Figure 1. The first case corresponds to $k < 0$ which will not result in a complete gap closure as in the above cases, but instead in a gap reduction maneuver. This is due to the faster exponential decay of the velocity $((1/k) - 1)$
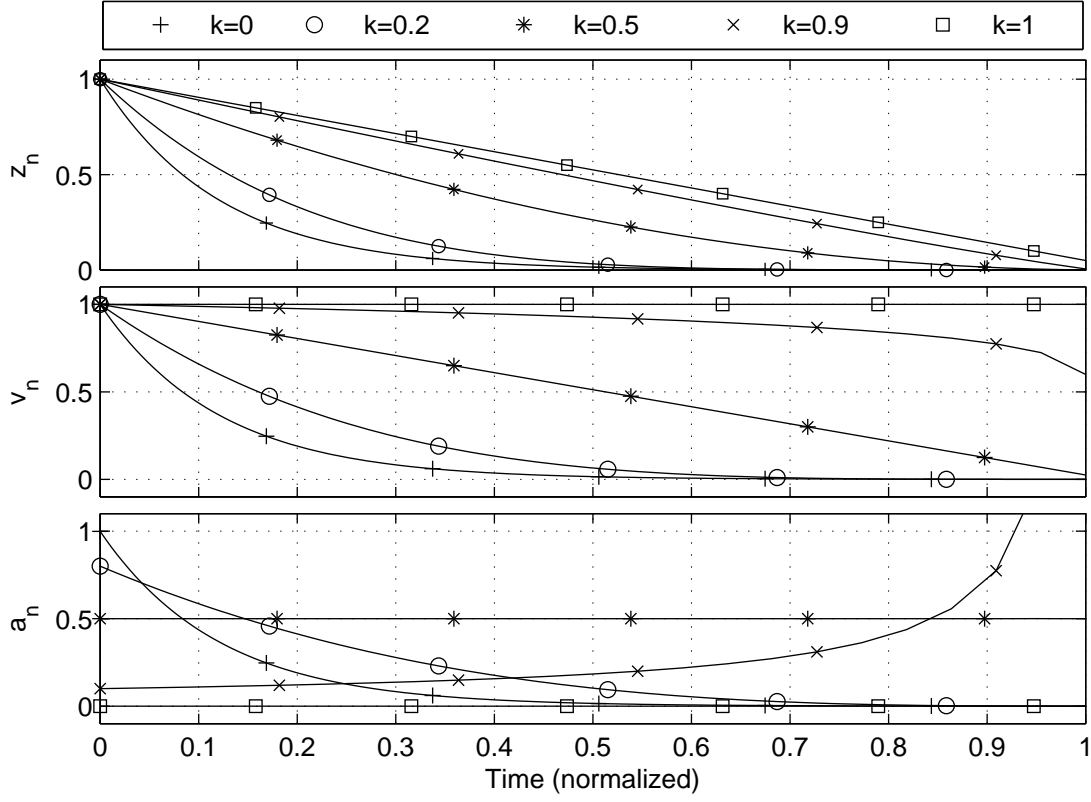
Fig. 1. Normalized object position, closing velocity and acceleration against normalized time under constant $\dot{\tau} = k$ for different values of k

compared to the exponential position decay $(1/k)$ for negative values of k. This means that the relative velocity is zeroed before the distance becomes zero, and the gap will be reduced but not fully closed. The second case corresponds to choosing $k = 0$ and is covered in section A, while the first case is covered in section B below.

A. Tau Theory Link to Constant Optic Flow Approach

Tau strategies are found in more developed species (like birds or humans) that require more flexible visual locomotion than insects (like bees) with their constant optic flow approach. So, the Tau strategy would be reasonably expected to address the challenges solved by the simpler strategy.

For asymptotic closure of a vertical gap during a vertical landing using the constant dilation approach [13], the image dilation ω_z, which is given by:

$$\omega_z = -\frac{\dot{z}}{z} \tag{4}$$

is held constant during the execution of the maneuver. Since the image dilation is the reciprocal of τ:

$$\tau = -\frac{1}{\omega_z} \tag{5}$$

then $\dot{\tau} = 0$ is an implementation of the Tau control strategy with $k = 0$. This predicts a soft touch landing with early initial deceleration as shown in Figure 1, demonstrating that the constant dilation strategy is a special case of the more general Tau strategy.

B. Tau Based Visual Control Applied to Vertical Takeoff and Landing (VTOL) Vehicles

Tau theory can be used to control the vertical dynamics of an aerial robot, or even a spacecraft. Because under the Tau strategy the choice of the constant $\dot{\tau} = k$ changes the dynamics of the gap closure, this allows the same strategy to be used to achieve different objectives.

a) Tau Based Visual Landing: In case of a VTOL platform like a quadrotor equipped with a downward looking camera, the vision system can visually register the value of Tau. Then in order to perform a landing maneuver, the generated vertical thrust is controlled in order to keep $\dot{\tau}$ constant at some chosen value $0 < k < 0.5$ so as to achieve a soft landing. Values closer to zero will result in an early deceleration followed by a flatter descent near the ground, while values closer to 0.5 will result in a linear reduction of the vertical velocity with time.

Because the value of Tau, not its rate of change, is the only value that can be registered visually, some kind of a differentiation filter should be used to estimate $\dot{\tau}$ for control purposes. A general Tau based control scheme is presented in Figure 2.
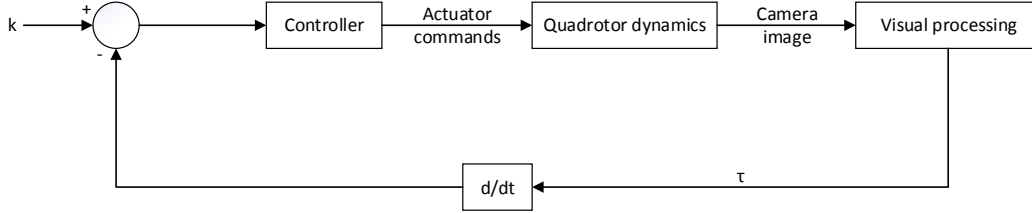

Fig. 2.   Tau based control scheme

Another application of the Tau strategy in this context is the hard contact landing achieved by choosing $0.5 < k < 1$. As mentioned above, this will practically result in a gap closure with a forward velocity residual. This velocity residual can be useful in docking maneuvers, for example. As hummingbirds use this mode for docking into flowers in mid air [22], a similar approach could be applied to aerial or space vehicles docking on a station. Yet another application might be a target knockdown similar to those performed by birds of prey when knocking prey down before catching them, however the use of the Tau strategy in this case has not been biologically observed.

b) Extension to Near-ground Hover and Altitude Hold: Choosing k to be a constant negative value has some useful applications, which have not been biologically validated or empirically observed. It can be seen from equations (3) that choosing negative values for k causes the velocity to decay exponentially by the power of $(1/k - 1)$ with respect to time. Additionally, the velocity v_z decay is always faster than the position z decay because $1/k - 1 < 1/k$ for negative values of k. This means that the relative velocity will reach zero before the gap is actually closed.

This closure profile can be used to approach some object without landing or touching it, possibly for inspection purposes. This can be useful for safe landing site identification or to observe a possible target of interest before the actual landing or an abort decision is taken. The chosen value of k reflects how far the flier wants to approach the ground; the closer the value of k to zero the closer the flier will approach the ground before the vertical velocity is zeroed and the maneuver effectively turns into an altitude hold. The same strategy can be exploited to command an immediate hover by setting $k \ll 0$.

It is important to note that although the vertical velocity v_z will decay faster than the position z in the case of $k < 0$, the maneuver will still theoretically finish with an asymptotic soft landing with zero position and velocity. However, due to the very long time it will take to touch down, the position change will be effectively negligible within practical time scales. Thus, this work uses the extension of Tau theory with $k < 0$ to maintain a distance from the ground in relaxed practical terms, rather than in the strict definition of altitude control. Hence, the terms altitude hold, and approach then stop, which are used in this text are interpreted in this context.

III. BODY-CENTRIC QUADROTOR MODEL

The quadrotor model presented here is similar to that developed in [30], and will be briefly demonstrated using the axes orientation used in this research. Two Cartesian coordinate frames are defined for the purpose of quadrotor modeling. The earth surface fixed frame with axes $\mathbf{1}_x^e, \mathbf{1}_y^e$ and $\mathbf{1}_z^e$ aligned with North, East and Down (NED) local directions respectively, which is safely assumed to be an inertial frame for the purposes of the slow and short flight of the quadrotor. The second frame is a body fixed frame with its origin at the body center of mass and axes $\mathbf{1}_x, \mathbf{1}_y$ and $\mathbf{1}_z$ aligned with forward, right (starboard), and down body orientations. The body and earth coordinate frames, motor numbering, and their positive rotation direction are illustrated in Figure 3.
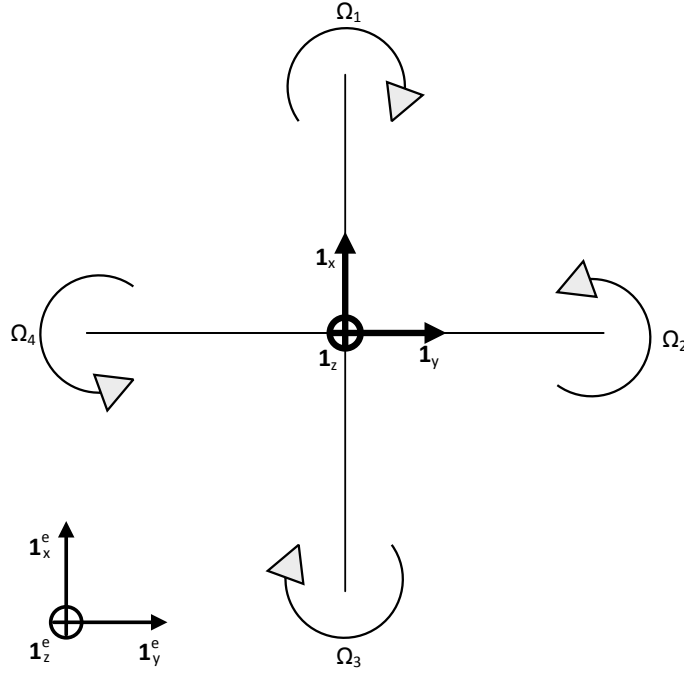
Fig. 3. Top view of the quadrotor showing the definition of coordinates frames, motor numbering and positive motor rotation direction. Axes $\mathbf{1}_z^e$ and $\mathbf{1}_z$ are pointing into the page

A. Attitude and Rotation Representation

The body attitude is represented (relative to the earth frame) by the right-handed rotation sequence (yaw, pitch, roll) with angles ψ, θ, ϕ about $\mathbf{1}_z$, $\mathbf{1}_y$, and $\mathbf{1}_x$ axes, respectively. These three rotations define the transformation matrix $R_{b/e}$.

Consequently, the quadrotor angular velocity in the earth frame $\boldsymbol{\omega}_{b/e}^e = [\dot{\phi}, \dot{\theta}, \dot{\psi}]$ and in body frame $\boldsymbol{\omega}_{b/e}^b = [p, q, r]$ are related as follows [31]:

$$\boldsymbol{\omega}_{b/e}^e = \begin{bmatrix} 1 & \tan(\theta)\sin(\phi) & \tan(\theta)\cos(\phi) \\ 0 & \cos(\phi) & -\sin(\phi) \\ 0 & \sin(\phi)/\cos(\theta) & \cos(\phi)/\cos(\theta) \end{bmatrix} \boldsymbol{\omega}_{b/e}^b \tag{6}$$

B. Quadrotor Body Dynamics

Using Newton's Euler formalism, the body dynamics are expressed in the body fixed frame as:

$$\begin{bmatrix} m\boldsymbol{I}_{3\times3} & \mathbf{0}_{3\times3} \\ \mathbf{0}_{3\times3} & \boldsymbol{I}_q \end{bmatrix} \begin{bmatrix} \dot{\boldsymbol{V}}^b \\ \dot{\boldsymbol{\omega}}_{b/e}^b \end{bmatrix} + \begin{bmatrix} \boldsymbol{\omega}_{b/e}^b \times m\boldsymbol{V}^b \\ \boldsymbol{\omega}_{b/e}^b \times \boldsymbol{I}_q\boldsymbol{\omega}_{b/e}^b \end{bmatrix} = \begin{bmatrix} \mathbf{F}^b \\ \boldsymbol{\tau}^b \end{bmatrix} \tag{7}$$

The quadrotor is assumed to be symmetric about its body principal axes which are assumed to coincide with the body frame. This assumption cancels all products of inertia and the inertia matrix becomes the diagonal matrix $\boldsymbol{I}_q = \mathrm{diag}(I_{xx},\ I_{yy},\ I_{zz})$.

The external forces acting on the quadrotor body are the weight force (mg) and the thrust forces generated by the four propellers T_i. Each thrust force is modeled as:

$$T_i = n\,\Omega_i^2,\ i = 1, 2, 3, 4 \tag{8}$$

and the total thrust force $T_a = T_1 + T_2 + T_3 + T_4$ is always aligned with the body $\mathbf{1}_z$ axis in the negative direction.

The total torque acting on the quadrotor is composed of the control torques and gyroscopic effect torque. Control torques $\boldsymbol{\tau}_x$, $\boldsymbol{\tau}_y$ that generate a positive rolling and pitching moment can be expressed as:

$$\begin{aligned} \boldsymbol{\tau}_x &= \ell(T_4 - T_2)\mathbf{1}_x \\ \boldsymbol{\tau}_y &= \ell(T_1 - T_3)\mathbf{1}_y \end{aligned} \tag{9}$$

The aerodynamic drag torque Q_i acting on propeller i is modeled as:

$$Q_i = d\Omega_i^2, \, i = 1, 2, 3, 4 \tag{10}$$

The total drag torque that generates a positive yawing moment is expressed as:

$$\boldsymbol{\tau}_z = d(\Omega_2^2 + \Omega_4^2 - \Omega_1^2 - \Omega_3^2)\mathbf{1}_z \tag{11}$$

Body angular rates induce a gyroscopic effect torque $\boldsymbol{\tau}_J$ on each of the rotating propellers due to rotor inertia J and the total imbalance Ω_{res} in the propeller angular velocities. $\boldsymbol{\tau}_J$ can be expressed as:

$$\boldsymbol{\tau}_J = J(\boldsymbol{\omega}_{b/e}^b \times \mathbf{1}_z)\Omega_{res} = \begin{bmatrix} J \, q \, \Omega_{res} \\ -J \, p \, \Omega_{res} \\ 0 \end{bmatrix} \tag{12}$$

where

$$\Omega_{res} = \Omega_2 + \Omega_4 - \Omega_1 - \Omega_3 \tag{13}$$

By defining the following variables:

$$\begin{aligned} U_1 &= (\Omega_1^2 + \Omega_2^2 + \Omega_3^2 + \Omega_4^2) \\ U_2 &= (\Omega_4^2 - \Omega_2^2) \\ U_3 &= (\Omega_1^2 - \Omega_3^2) \\ U_4 &= (\Omega_2^2 + \Omega_4^2 - \Omega_1^2 - \Omega_3^2) \end{aligned} \tag{14}$$

the quadrotor model dynamic equations $(\dot{p}, \dot{q}, \dot{r}, \dot{v}_x, \dot{v}_y, \dot{v}_z)$ expressed in the body fixed coordinates frame as well as the local earth attitude kinematics $(\dot{\phi}, \dot{\theta}, \dot{\psi})$ can be written as:

$$\begin{aligned} \dot{p} &= [q \, r \, (I_{yy} - I_{zz}) + J \, q \, \Omega_{res} + \ell \, n \, U_2] \, / \, I_{xx} \\ \dot{q} &= [p \, r \, (I_{zz} - I_{xx}) - J \, p \, \Omega_{res} + \ell \, n \, U_3] \, / \, I_{yy} \\ \dot{r} &= [p \, q \, (I_{xx} - I_{yy}) + d \, U_4] \, / \, I_{zz} \\ \dot{v}_x &= r \, v_y - q \, v_z - g \sin(\theta) \\ \dot{v}_y &= p \, v_z - r \, v_x + g \cos(\theta) \sin(\phi) \\ \dot{v}_z &= q \, v_x - p \, v_y + g \cos(\theta) \cos(\phi) - \, n \, U_1 \, /m \\ \dot{\phi} &= p + q \, \tan(\theta) \sin(\phi) + r \, \tan(\theta) \cos(\phi) \\ \dot{\theta} &= q \, \cos(\phi) - r \, \sin(\phi) \\ \dot{\psi} &= q \, \sin(\phi)/\cos(\theta) + r \, \cos(\phi)/\cos(\theta) \end{aligned} \tag{15}$$

IV. Control Scheme

As the quadrotor is open loop unstable and has fast rotational dynamics, the proposed control strategy is hierarchical in nature. A discrete-time Linear Quadratic tracker [32] is used to provide low-level stabilizing control to the quadrotor. This controller is designed on the basis of a Jacobian linearized dynamic model (15), excluding body velocity states v_x, v_y, v_z, about the equilibrium point $\boldsymbol{x}_{eq} = [0, 0, 0, 0, 0, 0]^T$, $\boldsymbol{u}_{eq} = [\Omega_h, \Omega_h, \Omega_h, \Omega_h]^T$.

The low-level controller takes as input a vector of references $\boldsymbol{y}_r = [\psi_r, a_{xr}, a_{yr}, a_{zr}]^T$. Its control vector is $\boldsymbol{u} = [\Omega_1, \Omega_2, \Omega_3, \Omega_4]^T$ and its state vector is $\boldsymbol{x} = [\phi, \theta, \psi, p, q, r]^T$. The low-level control law is given by

$$\boldsymbol{u}(n) = -\boldsymbol{K}\boldsymbol{x}(n) + \boldsymbol{F}\boldsymbol{y}_r(n+1) \tag{16}$$

where matrices $\boldsymbol{K}, \boldsymbol{F}$ are the state feedback and reference feed-forward gains respectively.

The low-level control is used to stabilize the fast rotational dynamics of the quadrotor and provides the ability to control translational dynamics by tracking a body acceleration and heading reference signal $\boldsymbol{y}_r = [\psi_r, a_{xr}, a_{yr}, a_{zr}]^T$. The high-level control, on the other hand, implements the proposed Tau based control strategy by commanding the low-level control with a suitable reference signal.

A. High-level Tau Strategy Control System

The first step towards achieving a realistic implementation of the Tau based control scheme shown in Figure 2 is to find a way to deal with the problems associated with obtaining $\dot{\tau}$ from the visually registered Tau. Numerically differentiating τ, which is normally noisy, is problematic. Using a low pass differentiation filter is challenging as the frequency content of τ is not constant, which may result in a conservative filter with a very low cut-off frequency. In this paper, a novel method is used to avoid estimating $\dot{\tau}$ altogether while still implementing the Tau strategy. This is done by formulating the Tau strategy in an integral form, which is possible because Tau based control will only be activated when performing the required task starting from some initial conditions.

The Tau strategy aims to hold $\dot{\tau} = k$ constant, hence by integration, the following law is obtained:

$$\tau_r(t) = k \, t + \tau_0 \tag{17}$$

where τ_0 is the integration constant which can be defined at the moment the Tau based control is engaged.. The visual variable Tau is made to track the reference $\tau_r(t)$ to achieve the same goal as defined originally.

Although the integral law (17) solves the τ differentiation problem, it still suffers from two other issues when applied to quadrotor automatic landing. First, from (1) it is clear that the gap will be closing only if τ is negative, which puts a constraint on $\tau_r(t)$ to span negative values only. Solving for t in (17) with the constraint $\tau_r(t) < 0$ results in two conditions. Firstly $\tau_0 < 0$, otherwise the control law will demand the gap to be opened (fly away from the ground) at $t = 0$. Secondly, t must satisfy

$$
\begin{aligned}
t &< -\frac{\tau_0}{k} \qquad \text{if} \ \ k > 0 \\
t &> -\frac{\tau_0}{k} \qquad \text{if} \ \ k < 0
\end{aligned}
\tag{18}
$$

which defines the time validity of the task or the theoretical maneuver execution time. If $\tau_0 < 0$ is satisfied then it is easy to show that the second case in (18) is always valid, whereas there is a limited time validity to complete the task for the first case in (18) to be satisfied. Furthermore, if $k = 0$, which is equivalent to the constant image dilation strategy, time t disappears in (17) and landing will be achieved as long as $\tau_0 < 0$.

The above analysis shows that the task execution time is determined by the choices of τ_0 and k. The choice of k has a direct effect on the maneuver's dynamics, as has been described in section II. On the other hand, the choice of τ_0 has an indirect effect due to its contribution to the task execution time. Choosing τ_0 to be equal to the estimated value of τ at the time of the maneuver initiation is possible as long as it is negative, i.e the vehicle is moving downwards. Choosing smaller or larger values of τ_0 than its estimated value will result in lengthening or shortening the maneuver execution time. In the case where the vehicle was hovering, the value of τ is not defined, and if the vehicle is moving upwards then $\tau > 0$ at the time of maneuver initiation, thus the estimated value of τ cannot be used. In these two cases, a suitable value $\tau_0 < 0$ has to be chosen such that the maneuver is feasible to complete in $-\frac{\tau_0}{k}$ seconds. Ideally, τ_0 and k should be chosen automatically by a higher level function in the control hierarchy, employing the awareness of the environment and knowledge of dynamical capabilities and the objective of the maneuver. In this work, however, these values have been chosen manually to explore their effect on the maneuver dynamics and aid comparison with the theoretical results.

Nevertheless, robustness issues might arise due to improper choice of τ_0. If (for any reason) the task does not finish in the specified time then the solution provided by equation (17) becomes invalid and will start to command the vehicle to fly away from the ground indefinitely. To address this issue, an automatic re-initiation of the task is performed each time the allowed task time runs out until successful completion or task abortion. The logic behind this solution comes from different observed cases where an animal or human reuses the same strategy (though not a Tau strategy) when temporary adverse environmental conditions make it difficult to achieve the intended task [33], [34]. Using this solution, the possibility that the control scheme will use a suitable (possibly estimated) value for τ_0 when the maneuver re-initiates is increased. This is because the vehicle will be moving in the downward direction, hence the value of τ_0 can be estimated.

The second problem is that the τ associated with the vertical gap is only defined if the vertical velocity v_z is non-zero. This causes the control system implementing (17) to exhibit singularities each time the vertical velocity becomes zero, which is expected to happen whenever the landing task is initiated from hover or if the quadrotor was initially moving in the upward direction. Fortunately the image dilation ω_z is defined for all values of vertical velocity. Taking the reciprocal of (17) results in:

$$\omega_{zr}(t) = -\frac{1}{k \, t + \tau_0} \tag{19}$$

and hence regulating the visually registered image dilation to track $\omega_{zr}(t)$ becomes equivalent to enforcing the original Tau strategy defined by $\dot{\tau} = k$. It should be noted that the solution provided by (19) is still subject to

time validity constraints defined in (18), which additionally ensures that the denominator of (19) cannot be zero, and such solution will always be valid as long as time validity is preserved. Figure 4 shows the differentiation-free singularity-free control scheme which is equivalent in goal to the control scheme shown in Figure 2 and which is experimentally tested in section V.
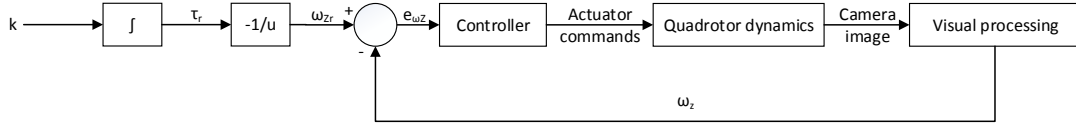

Fig. 4.   Differentiation-free dilation based control structure equivalent to constant $\dot{\tau}$ approach

B. Choice of Task Parameters

In the law defined by (19) there are two parameters k and τ_0 that can be chosen by the user. The choice of k has been discussed in detail in Section II. Parameter τ_0 controls the image dilation reference in the special case where Tau control reduces to constant dilation approach ($k = 0$). In this case, the image dilation reference becomes equal to $\omega_{zr} = -\frac{1}{\tau_0}$. Another influence of τ_0 is the theoretical execution time of the maneuver (18). Firstly, τ_0 must be chosen strictly negative as discussed in section IV.IV-A. Secondly, from (18) it is clear how smaller values of τ_0 result in a longer theoretical maneuver execution time. On the other hand, larger values for τ_0 shorten the maneuver execution time. The value of τ_0 can be manipulated to be larger or smaller than the registered value of Tau at the moment of task initiation to extend or shorten the task execution time, respectively.

C. Design of Visual Velocities Tracker

Based on the previous discussion, Tau is controlled by tracking a time varying image dilation reference signal $\omega_{zr}(t)$ using (19) and the proposed control scheme shown in Figure 4. The visual processing system runs at a constant rate with a sampling time T_{vs} and registers the value of image dilation $\omega_z(n)$ at a discrete time step n. The controller shown in Figure 4 aims to eliminate the dilation error $e_{\omega_z}(n)$ defined by:

$$e_{\omega_z}(n) = \omega_{zr}(n) - \omega_z(n) \tag{20}$$

which can be regulated by providing a suitable reference signal $a_{zr}(n)$ to the low-level control.

The simplest controller design to test the strategy is a PI type compensator where the proportional and integral actions are used to achieve fast response time and zero steady state error. The output of the compensator sets the vertical body acceleration reference $a_{zr}(n)$:

$$a_{zr}(n) = K_{P3} \; e_{\omega_z}(n) + K_{I3} \; \sum_{i=0}^{n} e_{\omega_z}(i) \tag{21}$$

where K_{P3} and K_{I3} are the proportional and integral actions gains, respectively. The low-level control is responsible for tracking the commanded acceleration.

In order to vertically land on a surface, it is preferable that no lateral relative velocity between the quadrotor and the landing surface exists at touchdown. To achieve this goal, a simple visual control can be used to cancel the ventral flows ω_x, ω_y while the vertical control is taking place. These ventral flows are defined by:

$$\omega_x = \frac{v_x}{z} \tag{22}$$

$$\omega_y = \frac{v_y}{z} \tag{23}$$

and are visually estimated by the visual processing system as demonstrated in the next section. A simple PI controller is used to eliminate ω_x, ω_y by providing the following low-level body acceleration reference signals:

$$a_{xr}(n) = -\left(K_{P2} \; \omega_x(n) + K_{I2} \; \sum_{i=0}^{n} \omega_x(i) \right)$$

$$a_{yr}(n) = -\left(K_{P1} \; \omega_y(n) + K_{I1} \; \sum_{i=0}^{n} \omega_y(i) \right) \tag{24}$$

K_{P1}, K_{P2} are proportional gains, and K_{I1}, K_{I2} are integral gains.

Finally, laterally stabilized landing can be achieved using pure visual information by providing a low-level vector reference signal $\boldsymbol{y}_r(n)$ comprising signals $a_{xr}(n), a_{yr}(n), a_{zr}(n)$ as defined by (21) and (24), to the low level controller. The heading reference component ψ_r of $\boldsymbol{y}_r$ is set constant to a predefined value to hold the vehicle heading while the maneuver is performed.

V. ESTIMATION OF VISUAL MOTION PARAMETERS

Optic flow or image velocities (u, v) can be described as a function of the camera six degrees of freedom ego-motion (three translational velocities v_x^c, v_y^c, v_z^c, and three angular velocities p^c, q^c, r^c), the depth of the observed point Z, and the focal length f as follows:

$$
\begin{aligned}
u &= -f\left(\frac{v_x^c}{Z} + q^c\right) + x\frac{v_z^c}{Z} + yr^c - x^2\frac{q^c}{f} + xy\frac{p^c}{f} \\
v &= -f\left(\frac{v_y^c}{Z} - p^c\right) + y\frac{v_z^c}{Z} - xr^c + y^2\frac{p^c}{f} - xy\frac{q^c}{f}
\end{aligned}
\tag{25}
$$

where the projection of the world coordinate point $\boldsymbol{P} \in \{(X, Y, Z) \in \mathbb{R}^3 : Z > 0\}$ onto the image plane gives the image point $\boldsymbol{p} \in \{(x, y) = (fX/Z, fY/Z) \in \mathbb{R}^2 : Z > 0\}$. The camera translational and angular velocities are given in the camera frame, which is rigidly attached to the camera where its $\boldsymbol{1}_x^c$, and $\boldsymbol{1}_y^c$ axes are aligned with the image horizontal and vertical directions, while the $\boldsymbol{1}_z^c$ axis is aligned with the optical axis pointing towards the scene.

The goal of the estimation task is not to deduce the actual ego-motion parameters (translational and angular velocities) but to find visual motion parameters, namely Focus of Expansion (FOE), the camera frame image dilation ω_z^c, and ventral flows ω_x^c, ω_y^c, which could be used directly in the control problem.

The adopted method is similar to that presented in [35] but it has been modified to make use of the IMU information available on the quadrotor. During this research, the authors found that the reliability of the visual parameter estimation method presented in [35], which does not use IMU data, is not satisfactory under experimental conditions. This is due to the considerable difference in the visual processing rate, which is capped by the limited processing capabilities, compared to the fast rotational dynamics of the quadrotor. Therefore, in addition to the original assumption of the scene being planar, the rotational components of the flow are assumed to have been removed, which can be done using IMU information. This information is commonly available on UAV and MAV platforms, so this is a reasonable assumption.

It worth mentioning that a similar visual algorithm has been presented in [36] to estimate the required visual motion parameters $(\omega_x, \omega_y, \omega_z)$ in addition to the surface slope. This algorithm estimates the variables of interest from the first and second derivatives of the estimated model of the optic flow field at the center of the image. Both the visual method presented in this paper and the one demonstrated in [36] stem from the seminal work of [37]. The choice of the simpler method presented here is made as the Tau theory based landing does not work with inclined surfaces, as each point will have a distinct time-to-contact, and estimating the surface slope will not contribute to the Tau based vertical control, which is the focus of this paper.

A. Simultaneous Visual Motion Parameter Estimation

By removing the rotational component of the optic flow from (25) the translational components of the optic flow u_T, v_T can be expressed as:

$$
\begin{aligned}
u_T &= -f\frac{v_x^c}{Z} + x\frac{v_z^c}{Z} \\
v_T &= -f\frac{v_y^c}{Z} + y\frac{v_z^c}{Z}
\end{aligned}
\tag{26}
$$

In order to rewrite equation (26) in terms of the visual motion parameters $\omega_x^c, \omega_y^c, \omega_z^c$, one has to note that $v_z^c = -\dot{Z}$, thus, using (4), the image dilation can be written as:

$$
\omega_z^c = \frac{v_z^c}{Z}
\tag{27}
$$

Using (27) and definitions in (22) and (23), equation (26) can be written in terms of the visual motion parameters as:

$$
\begin{aligned}
u_T &= -f\omega_x^c + x\omega_z^c \\
v_T &= -f\omega_y^c + y\omega_z^c
\end{aligned}
\tag{28}
$$

Additionally, the image coordinates of the FOE x_{foe}, y_{foe} can be calculated from

$$x_{foe} = \frac{v_x^c}{v_z^c}$$
$$y_{foe} = \frac{v_y^c}{v_z^c} \tag{29}$$

which only exists when $v_z^c \neq 0$.

Since there are plenty of points where the optic flow can be evaluated, then it is possible to model the observed optic flow by means of a suitable parametric model. Thus, the required motion parameters can be simultaneously calculated from the optic flow model parameters.

The translational components (28) can be represented by the following model:

$$u_T = a_1 + a_2 x$$
$$v_T = a_3 + a_2 y \tag{30}$$

Then, optic flow estimates at multiple points are used to form a least squares regression problem. Thus (30) can be written in regression form as follows:

$$\begin{bmatrix} u_{T1} \\ v_{T1} \\ u_{T2} \\ v_{T2} \\ \vdots \\ u_{Tn} \\ v_{Tn} \end{bmatrix} = \begin{bmatrix} 1 & x_1 & 0 \\ 0 & y_1 & 1 \\ 1 & x_2 & 0 \\ 0 & y_2 & 1 \\ \vdots & \vdots & \vdots \\ 1 & x_n & 0 \\ 0 & y_n & 1 \end{bmatrix} \begin{bmatrix} a_1 \\ a_2 \\ a_3 \end{bmatrix} \tag{31}$$

which can be solved using least-squares to find the estimated model parameters $\hat{a}_1, \hat{a}_2, \hat{a}_3$. Then the camera frame image dilation ω_z^c, ventral flows ω_x^c, ω_y^c, and the FOE location x_{foe}, y_{foe} can be found from the estimated model parameters as follows:

$$\omega_z^c = \hat{a}_2$$
$$\omega_x^c = -\frac{\hat{a}_1}{f}$$
$$\omega_y^c = -\frac{\hat{a}_3}{f}$$
$$x_{foe} = -\frac{\hat{a}_1}{\hat{a}_2} \tag{32}$$
$$y_{foe} = -\frac{\hat{a}_3}{\hat{a}_2}$$

The camera is attached to the quadrotor body such that the $\mathbf{1}_z^c$ axis coincides with the body $\mathbf{1}_z$ axis and the camera $\mathbf{1}_x^c, \mathbf{1}_y^c$ axes are rotated with angle ψ_c about the body $\mathbf{1}_z$ axis with respect to body axes $\mathbf{1}_x, \mathbf{1}_y$, respectively. Using this arrangement, the image dilation in the camera and the body frame are equal $\omega_z = \omega_z^c$, whereas the ventral flows in the body and the camera frame are related as follows:

$$\begin{bmatrix} \omega_x \\ \omega_y \end{bmatrix} = \begin{bmatrix} \cos(\psi_c) & -\sin(\psi_c) \\ \sin(\psi_c) & \cos(\psi_c) \end{bmatrix} \begin{bmatrix} \omega_x^c \\ \omega_y^c \end{bmatrix} \tag{33}$$

The visual variables ω_x, ω_y, and ω_z are used by the high-level control system demonstrated in section III.

B. Outlier Rejection

The proposed method for the estimation of the visual motion parameters has been shown to produce quite accurate results in simulation [35]. However, before these estimates can be used in the control scheme described in section III, some challenges need to be addressed, as the raw estimates obtained from (32) can exhibit outliers which may occur due to the temporary violation of assumptions made by the optic flow method employed, and also due to the noisy nature of digital visual information. Such outliers would affect control performance if left unchanged.

To address this issue, the outliers need to be eliminated in real-time to enhance the robustness of the estimation. The median filter is a good robust statistical offline filter that can be used for outlier rejection. The running version of the median filter presented in [38] is used here for the purpose of outlier rejection where the median is replaced with a running median over a window of previous values.

C. IMU-aided Estimation of Visual Motion Parameters

Even with the fast real-time method presented here, the visual processing update rate is low when compared to the fast dynamics of the vehicle. To be able to use a high level control system with a sampling rate that is higher than the visual sampling rate, it is necessary to estimate the visual parameters between the sampling instants of the visual system. Moreover, after outlier rejection, the resulting estimates will still contain noise. Both inter-sample estimation and noise filtering can be achieved using an appropriate stochastic model-based estimation algorithm, such as a Kalman filter.

In order to develop a dynamic filter for the visual motion parameters, the dynamic model of $(\omega_x, \omega_y, \omega_z)$ is derived below. If a downward looking camera is rigidly mounted under a quadrotor, the height of the quadrotor z and the scene depth at the center of the image Z are related by the attitude angles. Under the assumption of small attitude angles, it is possible to use the approximation $z \approx Z$.

Let the state x_d be defined as follows:

$$x_d = \frac{1}{z} \tag{34}$$

Taking its time derivative gives:

$$\dot{x}_d = -\frac{\dot{z}}{z^2} \tag{35}$$

which, using the definition of image dilation (4), $\dot{x}_d$ can be written as:

$$\dot{x}_d = \omega_z x_d \tag{36}$$

Taking the time derivative of (22) and assuming that $z \neq 0$ gives:

$$\dot{\omega}_x = \frac{\dot{v}_x}{z} - \frac{\dot{z}}{z}\frac{v_x}{z} \tag{37}$$

The dynamic equations of body velocities, including $\dot{v}_x$, are given in the derived quadrotor body-centric dynamic equations (15). Noting that the acceleration component in the $\mathbf{1}_x$ axis of the body frame is $a_x = -g\sin(\theta)$, then $\dot{\omega}_x$ can be written as

$$\dot{\omega}_x = r\frac{v_y}{z} - q\frac{v_z}{z} + \frac{a_x}{z} - \frac{\dot{z}}{z}\frac{v_x}{z} \tag{38}$$

which can be described in the following form using definitions in (22),(23),(4), and (34)

$$\dot{\omega}_x = r\omega_y - q\omega_z + \omega_x\omega_z + a_x x_d \tag{39}$$

Given that the body starboard and downward acceleration components can be written as $a_y = g\cos(\theta)\sin(\phi)$ and $a_z = g\cos(\theta)\cos(\phi) - T_a/m$, respectively, the equations for $\dot{\omega}_y$ and $\dot{\omega}_z$ can be similarly derived and shown to be:

$$\dot{\omega}_y = p\omega_z - r\omega_x + \omega_y\omega_z + a_y x_d \tag{40}$$

$$\dot{\omega}_z = q\omega_x - p\omega_y + \omega_z^2 + a_z x_d \tag{41}$$

Using equations (39),(40),(41) and (36), the dynamic system for the visual motion parameters defined by the state vector $\boldsymbol{x}_f = [\omega_x, \omega_y, \omega_z, x_d]^T$ can be used to design a nonlinear Kalman filter. This will help both filtering the measurement noise and predicting the visual motion parameters at a higher rate to allow tighter high-level control. Similar data fusion has strong biological evidence and the fusion process has been found to have significant influence on the perception of self-motion in animals and humans. Visual and non-visual cues, such as gravito-inertial senses, proprioception and efferent copy all play a collaborative role in forming the perception of motion [39]. Not only does the brain handle different sensors, it also builds an estimation or expectation based on their information. This is supported by the fact that a mismatch between the expected and received motion cues can trigger what is known as motion sickness as shown in [40], where it is suggested that the Kalman filter functionally resembles the way the brain can handle multiple information sources and keep functioning when the quality of some of this information deteriorates.

The Unscented Kalman Filter (UKF) [41] has been proposed as a nonlinear extension to the Kalman filter. The filter exploits the unscented transformation to propagate the states and covariance matrices without the need to linearize the system as with the Extended Kalman Filter (EKF). The UKF has been shown superior to the EKF in term of convergence and accuracy when dealing with highly nonlinear systems [42]. Here, a discrete time UKF filter is designed. First, the UKF state vector $\boldsymbol{x}_f = [\omega_x, \omega_y, \omega_z, x_d]^T$, the input vector $\boldsymbol{u}_f = [p, q, r, a_x, a_y, a_z]^T$ provided by the IMU, and measurement vector $\boldsymbol{y}_f = [\omega_x, \omega_y, \omega_z]^T$ provided by the vision system are defined. Then the system dynamics in (39),(40),(41) and (36) are discretized (using fixed step Euler's method) to be used

TABLE I

PARAMETERS OF THE QUADROTOR NONLINEAR MODEL OBTAINED USING SYSTEM IDENTIFICATION

Parameter	Identified value
I_{xx}	1.21×10^{-2}
I_{yy}	1.355×10^{-2}
I_{zz}	2.179×10^{-2}
J_r	1.143×10^{-4}
n	2.256×10^{-5}
d	3.679×10^{-7}

by the discrete filter. The UKF produces filtered estimates $\hat{\boldsymbol{x}}_f$ at the same rate as the visual measurements $\boldsymbol{y}_f$. The numerical integration of the sigma points between visual sampling instants define N intermediate nodes, at which the weighted mean values of the propagated sigma points are calculated. These weighted mean values, which are obtained at a higher rate than the visual sampling rate, are used as state estimates $\tilde{\boldsymbol{x}}_f$ by the high level control system. This provides the control laws defined in (24) and (21) with their controlled signal $[\omega_x, \omega_y, \omega_z]$ using the estimated states $\tilde{\boldsymbol{x}}_f$, which enables a smoother control at a higher rate than the case when raw visual measurements are used.

The designed UKF uses a constant process covariance matrix $\boldsymbol{Q}_f$ that can be tuned manually to account for the unmodeled input noise and system dynamics. The measurement noise covariance, on the other hand, is time variant and is defined as $\boldsymbol{R}_f = \text{diag}(\frac{1}{\sigma_v^2}, \frac{1}{\sigma_v^2}, \frac{1}{\sigma_v^2})$ where σ_v is calculated from the root mean square (RMS) of the residuals of the optic flow fitting process in the model presented in section IV.A. Lastly, as the state x_d is strictly positive, then this condition is enforced in the filtering process. The method suggested by [43] is used by which the generated sigma points are clipped according to the state constraint. In contrast to the EKF, state clipping in the UKF is reflected on the propagated covariance reducing the clipped variable uncertainty in the unfeasible region. This gives another advantage of using the UKF over the EKF here.

VI. EXPERIMENTAL RESULTS

A. Experimental Platform

The Pelican quadrotor by Ascending Technologies GmbH is used in the experiments discussed below. The Pelican has a variety of sensors onboard, from which only the IMU (3-axes accelerometers and rate gyroscopes), the Attitude and Heading Reference System (AHRS) attitude estimations, and one downward looking camera that has 720×480 pixels and 49 degrees of vertical field of view have been used in the implementation of the control system. A downward facing ultrasonic range sensor is fitted to log the vehicle height during the experiment for analysis only and has not been used in the control system. It is worth mentioning that the height data collected from the ultrasonic sensor were very noisy and contain more than 50% outliers. These data are processed offline by a combination of mathematical closing and opening morphological operations and then smoothed by interpolating with smoothing splines. The splines and their first derivative are then evaluated to obtain an estimation of the quadrotor height and vertical velocity for analysis and comparison purposes.

The system is composed of three main components; the visual motion parameters registration system, the IMU-aided visual filtering subsystem, and the high and low level control systems. The visual motion parameters registration is implemented using OpenCV and runs on the Pelican on-board embedded computer (1.86GHz Intel Core Due2 processor), which has the camera connected to it. The visual motion parameters are registered at a rate of 20Hz then filtered through the running median filter. A serial communication link is utilized to send the visual motion parameters back to the Advanced RISC Machine (ARM7) processor where the IMU-aided filtering and control systems are implemented. The IMU-aided filtering and the high-level control run at 100Hz, while the low-level control runs at 1KHz and uses the onboard AHRS to estimate its state vector.

After collecting experimental flight data from the Pelican quadrotor, the Prediction Error Method (PEM) [44] was employed to find the parameter values for the dynamic model (15), which are given in Table I.

The values of the high-level controller gains $(K_{P1}, K_{I1}, K_{P2}, K_{I2}, K_{P3}, K_{I3})$ and the UKF process noice covariance matrix $\boldsymbol{Q}_f$ have been manually tuned to achieve reasonable performance. These values as well as the values of the low-level controller gains $\boldsymbol{K}$ and $\boldsymbol{F}$ are given in the appendix.

B. Visual Parameter Estimation

The performance of the visual parameter estimation method described in section IV is presented in Figure 5, which compares the output of the RM outlier filter and the output from the UKF filter against the raw values of

image dilation ω_z. The data is collected from an outdoor free flight over medium length grass. There are three cases to show in Figure 5. In the first case, the raw visual estimates contain some outliers as seen at seconds 320, 322, 335, and 337; however, these outliers have been successfully rejected by the RM filter. This shows the effectiveness of the RM filter in rejecting individual outliers. In the second case, the outliers in the raw visual estimates are not rejected by the RM filter as observed at second 340. The RM filter has been adapting to large magnitude changes that took place between seconds 225 and 340, so when an outlier appeared after these changes it has been accepted by the RM filter. Nevertheless, the UKF managed to filter the accepted outlier due to its access to the more reliable IMU information. Lastly, in the case of operational visual noise, which is present between seconds 342 and 350, the UKF managed to filter that noise and provide a smooth and reliable signal for the control system to operate on.
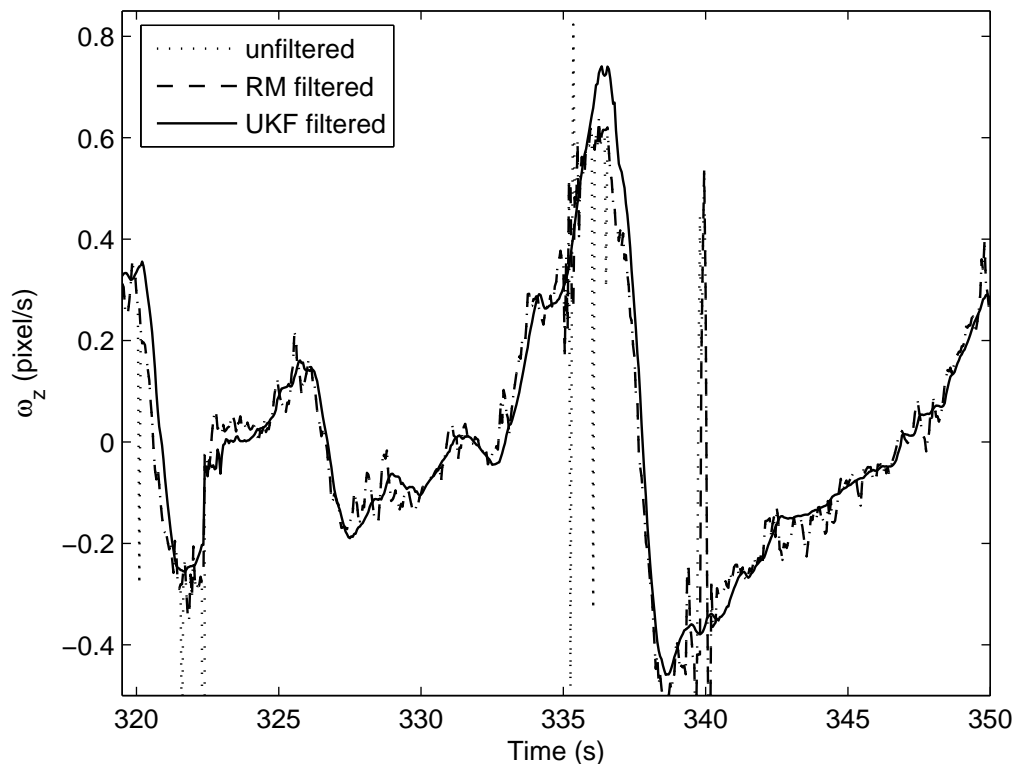
Fig. 5. Comparing unfiltered, Running Median (RM) filtered, and UKF filtered image dilation in free flight

C. Autonomous Tau Based Control Experiments

Autonomous flight experiments were performed indoors where the ground was covered with a $5\text{m} \times 5\text{m}$ print of randomly assembled lunar images taken by the personal telescope of Wes Higgins [1], as shown in Figure 6. The experiments were performed in moderate indoor lighting were the shadow of the quadrotor appears in the scene occasionally only near the ground. The textures in the scene were enough to identify 40 image features for optic flow estimates at a height of 5 m, and no less than 5 features at touch down. Although brief sharp light changes or loss of visual features can be tolerated using the proposed RMF and the IMU aided visual filter, extensive tests in a variety of visual conditions is outside the scope of this paper.

The quadrotor is first flown manually for at least 10 seconds for the visual motion parameters filter to converge, then the required autonomous visual control mode is engaged by a switch on the remote controller. A total of six experiments are shown here; the first experiment demonstrates the autonomous visual landing achieved by the Tau strategy using a maneuver constant of $k = 0.2$ starting from height $z_0 = 4$ m and downward vertical velocity $v_{z_0} = 0.77$ m/s. The second experiment is performed from similar initial conditions ($z_0 = 4.6$ m and $v_{z_0} = 0.88$ m/s) but using a different maneuver constant $k = 0.45$. The height and vertical velocity for experiments 1 and 2 are shown in Figure 7 and Figure 8, respectively.

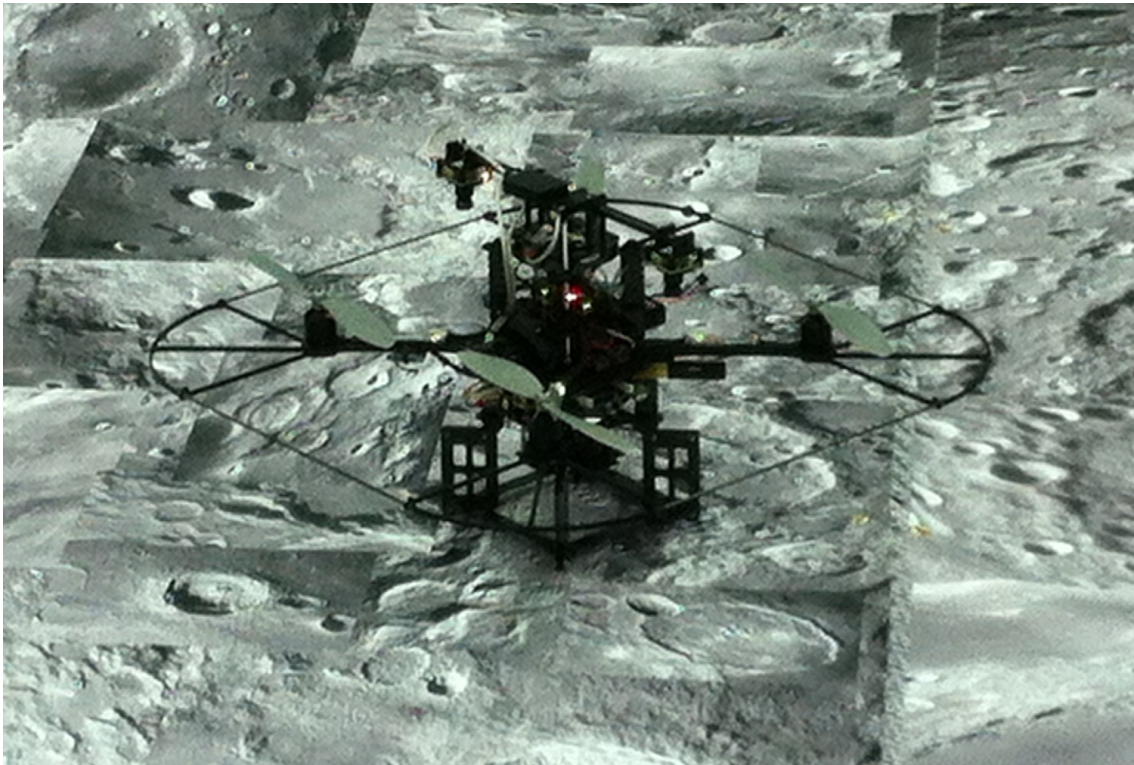[1]http://higginsandsons.com/astro/

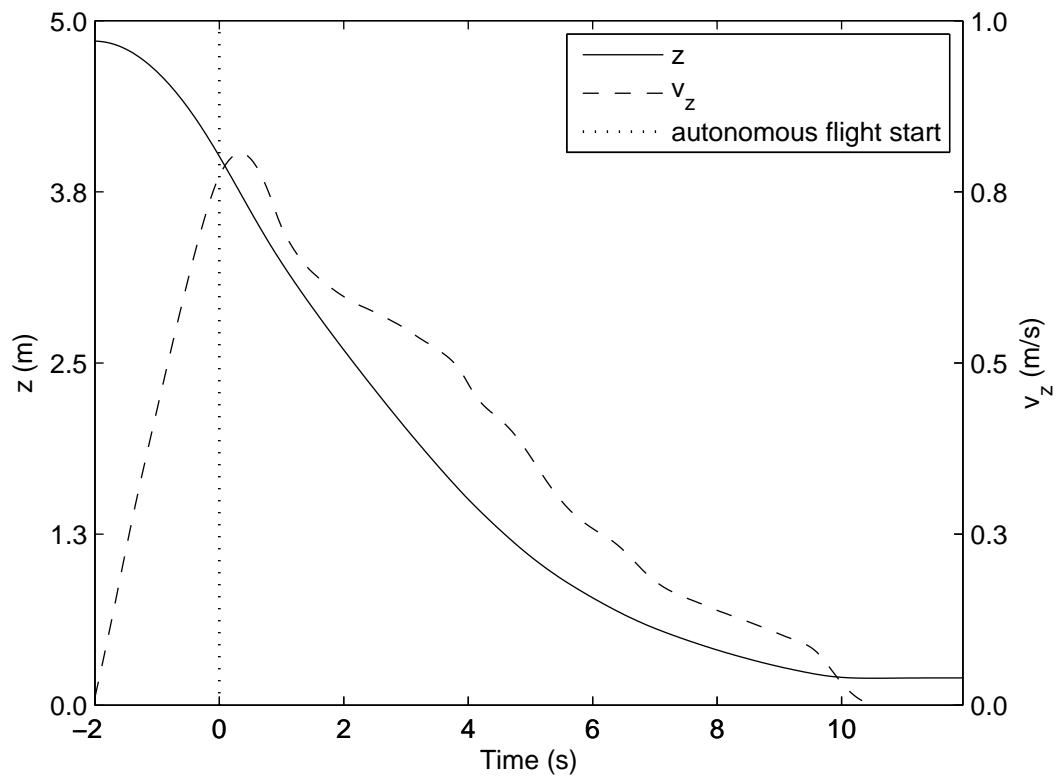Fig. 6. The Pelican quadrotor helicopter on a printed sheet of randomly assembled lunar images

Fig. 7. Height and vertical velocity of the quadrotor performing autonomous landing with k = 0.2

In the second experiment, the controlled signal τ is plotted against the reference signal τ_r as shown in Figure
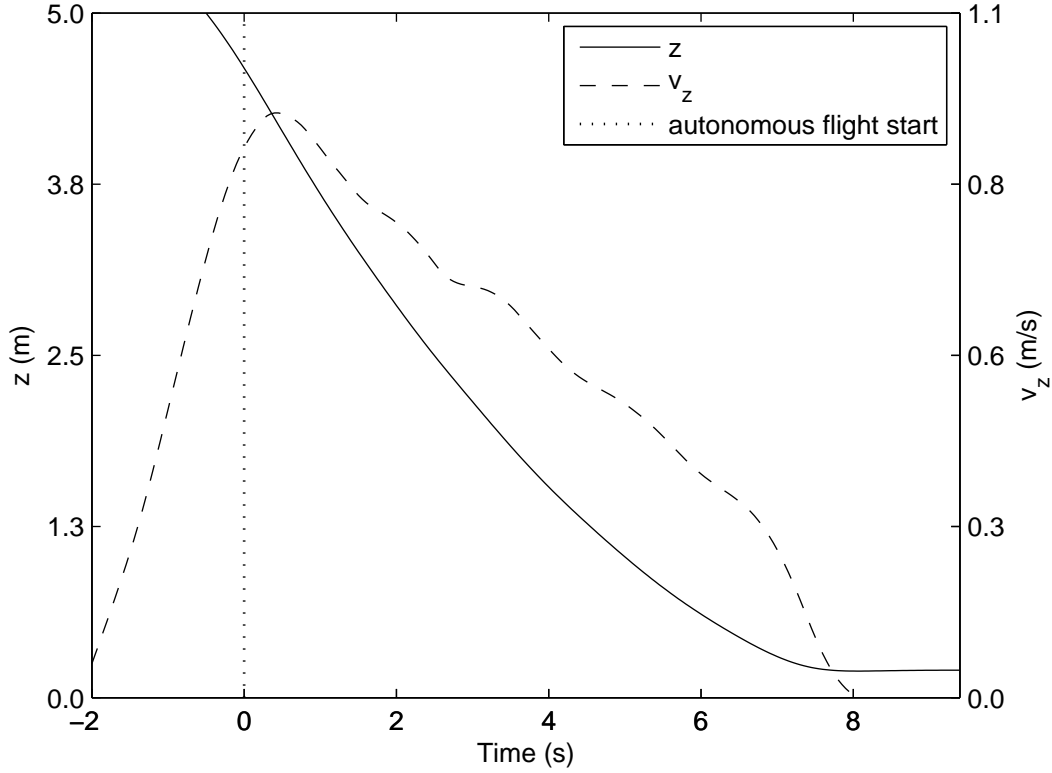
Fig. 8.   Height and vertical velocity of the quadrotor performing autonomous landing with k = 0.45

9. The reference signal is generated using Tau theory while the controlled signal is visually estimated using the proposed visual estimation and filtering scheme. Note that the value of τ becomes undefined at touch down, which took place at around 8 seconds. This explains the disparity between the reference and controlled signal in Figure 9 after touchdown. A sample set of the processed onboard images is shown in Figure 10 during a Tau based landing with $k = 0.45$. Note that the lateral displacement of the landing point is minimal. Note also presence of the quadrotor's shadow near the ground as in the last image.

The third and fourth experiments are presented to demonstrate the ability of the proposed control scheme to tolerate changes in the initial conditions of the maneuver. These experiments perform the same goal as in experiment 2 to land with $k = 0.45$, but experiment 3 starts from hover at $z_0 = 5.42$ m with a low vertical downward velocity $v_{z_0} = 0.02$ m/s, while experiment 4 starts while the quadrotor is flying upwards from $z_0 = 3.69$ m with an upward vertical velocity of $v_{z_0} = 0.66$ m/s. With zero or upward velocity the value of τ_0 becomes positive and the guidance law (17) becomes invalid, thus a value of $\tau_0 = -4$ has been chosen to start the maneuver. The height and vertical velocity profiles of experiments 3 and 4 are shown in Figures 11 and 12, respectively.

The last two experiments demonstrate the extension of the Tau strategy to perform ground approach maneuvers. In the fifth experiment, the quadrotor was at height $z_0 = 2.31$ m with a very low vertical velocity when the autonomous maneuver was engaged with $k = -10$. In the sixth experiment, the maneuver was engaged with similar initial conditions ($z_0 = 2.31$ m and $v_{z_0} = 0.06$ m/s) but with $k = -1.5$. Height and vertical velocity profiles for both experiments are shown in Figures 13 and 14, respectively.

Unfortunately, the experiment demonstrating a landing with a hard contact (using $0.5 < k < 1$ as presented in section II) is not safe to perform with the current experimental setup as there is a high risk of damaging the quadrotor. However, when the system was simulated, it was possible to obtain successful results performing the previous cases as well as the hard contact case. The simulation system and the experimental system share most software components including the control system implementation as well as visual processing and filtering implementations. In the simulations, the non-linear model equations given in (15) are integrated with a 4th order Runge-Kutta method and effectively replaces the quadrotor. The state vector obtained by integrating the quadrotor model is contaminated by Gaussian random values with the corresponding means and standard deviations values to the biases and standard deviations of the IMU gyroscopes and accelerometers evaluated experimentally. To simulate the camera, a 3D scene of the environment is generated by Virtual Reality Modeling Language (VRML)
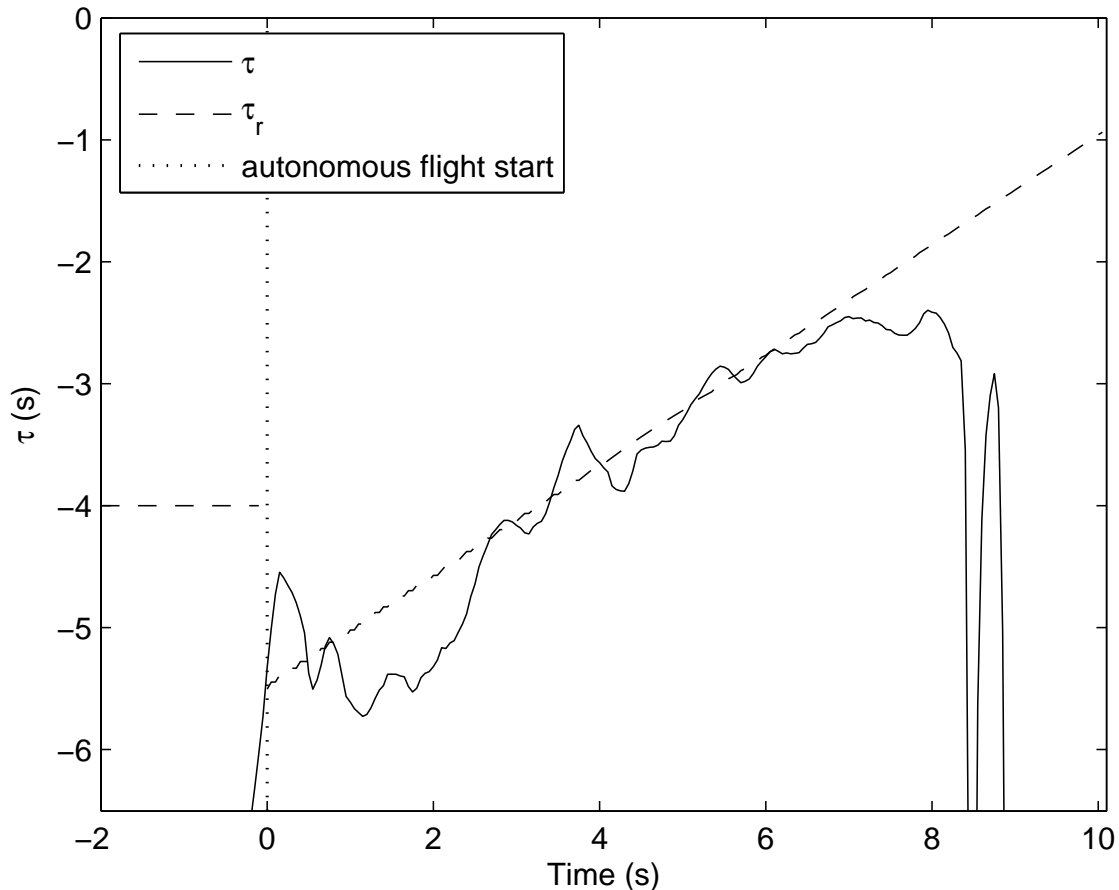
Fig. 9. The actual and reference values of the controlled variable τ when the quadrotor is performing autonomous soft landing with k = 0.45

and rendered at the same rate as the camera frame rate with the same camera projection properties (same field of view and image resolution). To achieve a hard contact landing, the maneuver constant was chosen to be $k = 0.85$. Height and vertical velocity are shown in Figure 15. As predicted theoretically, the maneuver ended when the quadrotor touched the ground with a velocity residual of -0.75 m/s approximately.

The total number of soft landing experiments, including those shown in this section, are 22 experiments, 9 of them are performed with $k = 0.2$ and 13 experiments are performed with $k = 0.45$. The data for these experiments are used for statistical analysis of the results presented in the next section.

VII. DISCUSSION

It is clear how the proposed Tau visual guidance strategy and the control scheme were able to achieve the different goals of the three sets of performed experiments. In the landing experiments 1 and 2, the quadrotor successfully performed visual autonomous landing with a soft contact and a very low velocity at touch down. Experiments 3 and 4 successfully performed autonomous soft contact visual landing from different initial conditions than what the original Tau theory proposes. And finally experiments 5 and 6 successfully achieved an autonomous ground approach maneuver using the proposed extension of the Tau strategy where the height is reduced for a brief period of time before the quadrotor starts hovering while awaiting further commands.

Some common behavior can be noticed across all experiments. Firstly, the final height above the ground is always 0.2 m as this is the minimum value the onboard ultrasonic range sensor can register. However, the landing gear lifts the quadrotor off the ground by a similar distance. In addition to that, the maneuvers did not terminate with zero vertical velocity as predicted by the theory because of the effect of the camera elevation. As the camera is mounted on the quadrotor about 0.3 m above the ground and due to the existence of the landing gear, the visual gap to the ground can never reach zero and the visual control system will keep demanding the quadrotor to move further down, which explains the small velocity residual at touchdown. Nonetheless, this residual has been found to be very small (below 0.08 m/s approximately) and the quadrotor still performs safe landings in all cases.

(a) z=4.5 m, t=0 s

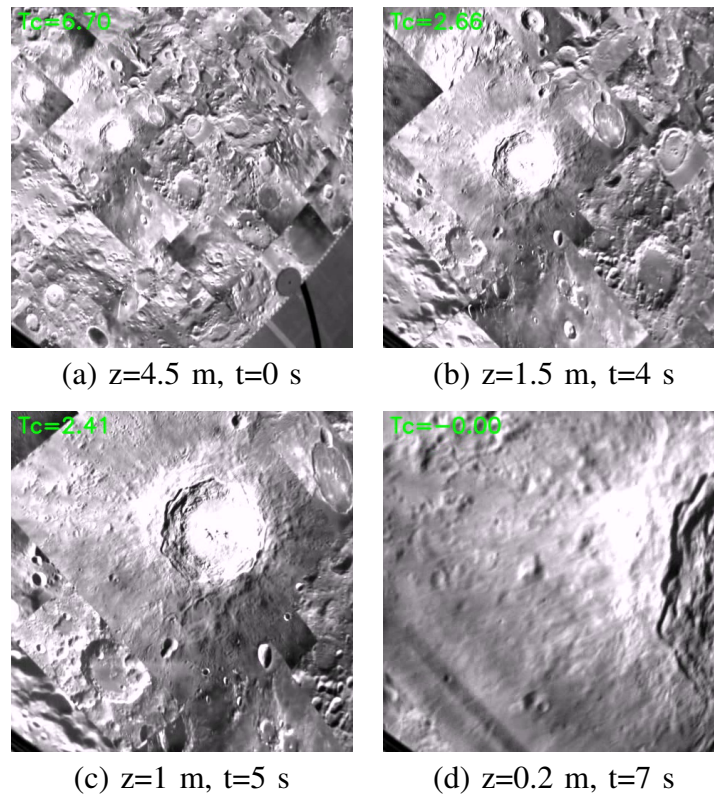(b) z=1.5 m, t=4 s

(c) z=1 m, t=5 s

(d) z=0.2 m, t=7 s

Fig. 10. Sample set of onboard images captured while landing using the proposed methods. Height and time are approximate.
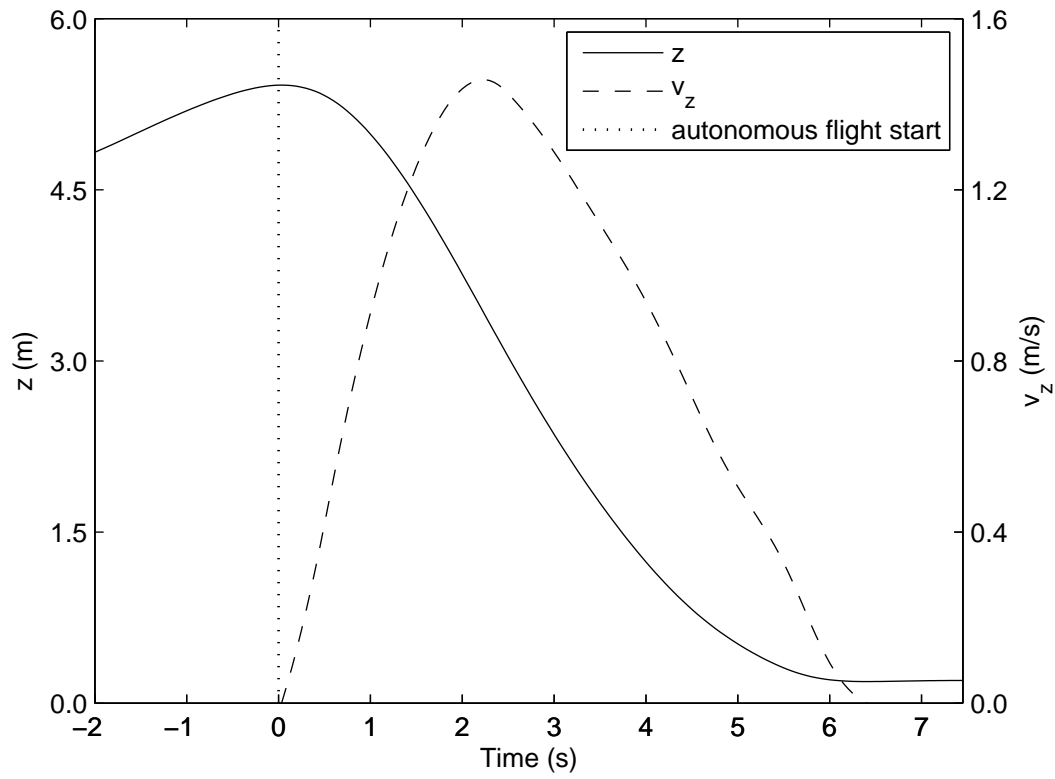

Fig. 11. Height and vertical velocity of the quadrotor performing autonomous landing with k = 0.45 from hover
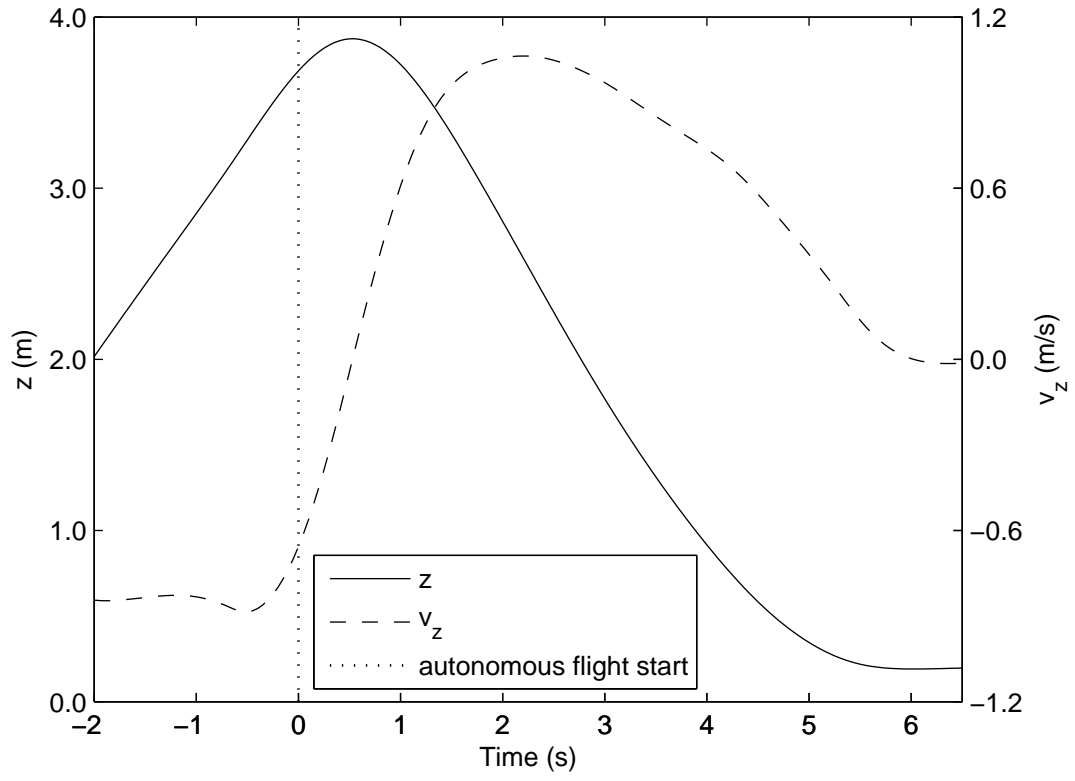
Fig. 12.   Height and vertical velocity of the quadrotor performing autonomous landing with k = 0.45 starting from upward motion
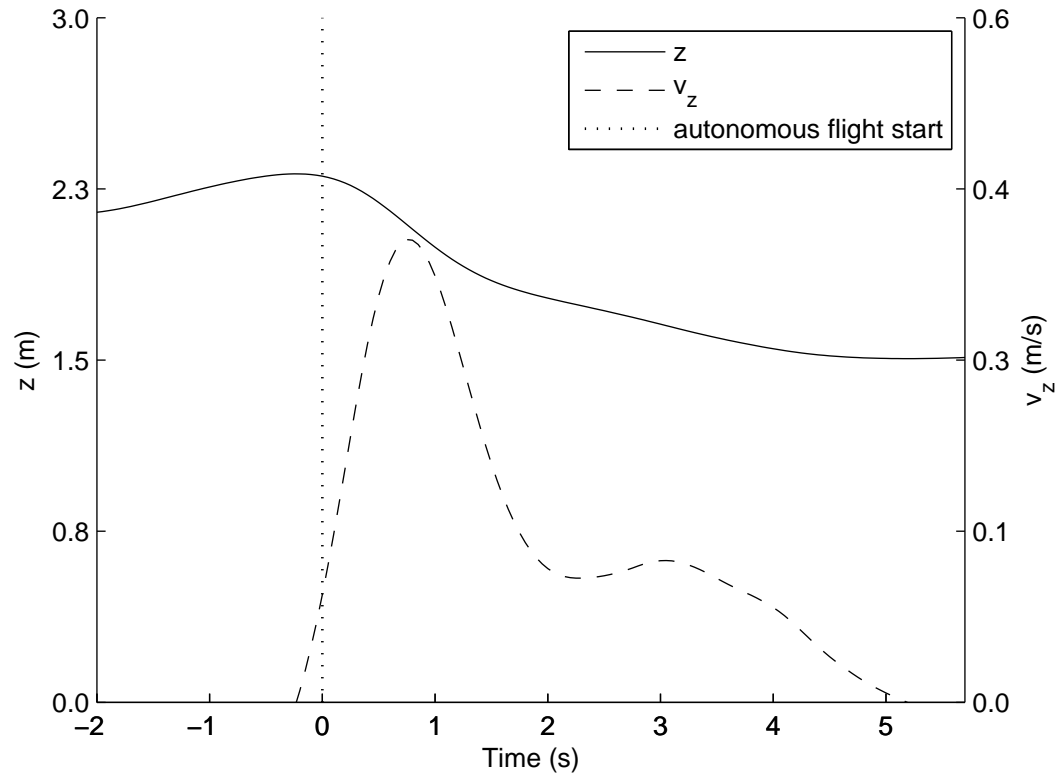

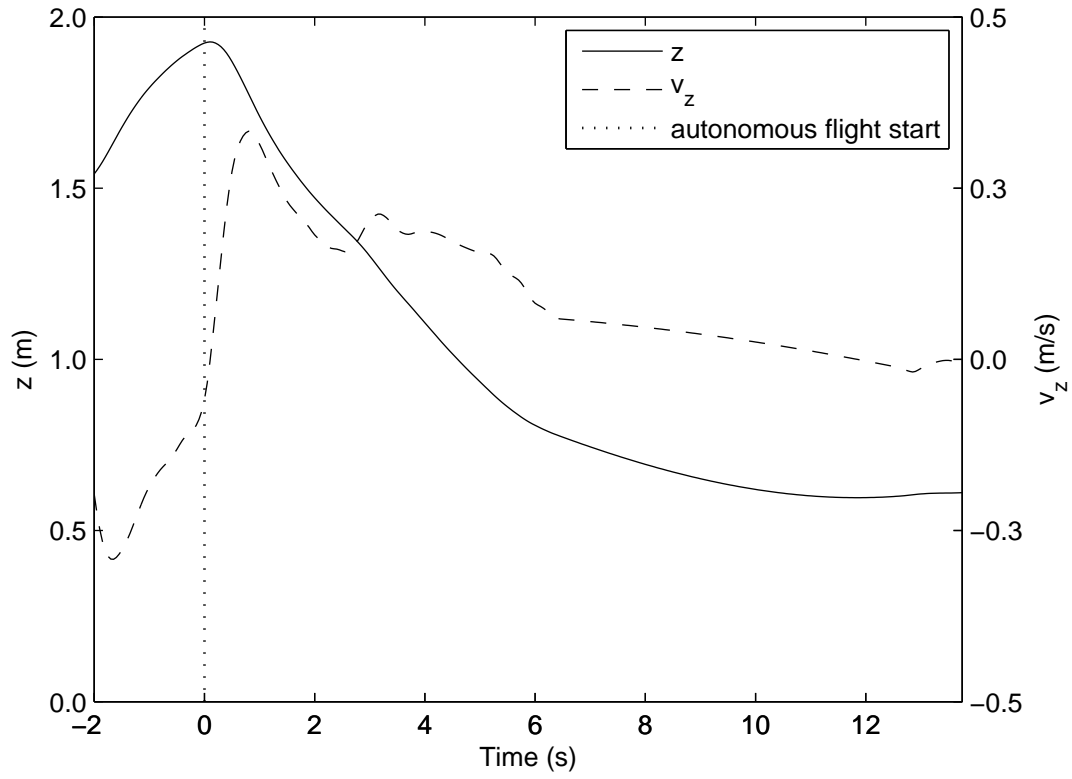Fig. 13.   Height and vertical velocity of the quadrotor performing autonomous ground approach with k = -10

Fig. 14. Height and vertical velocity of the quadrotor performing autonomous ground approach with k = -1.5
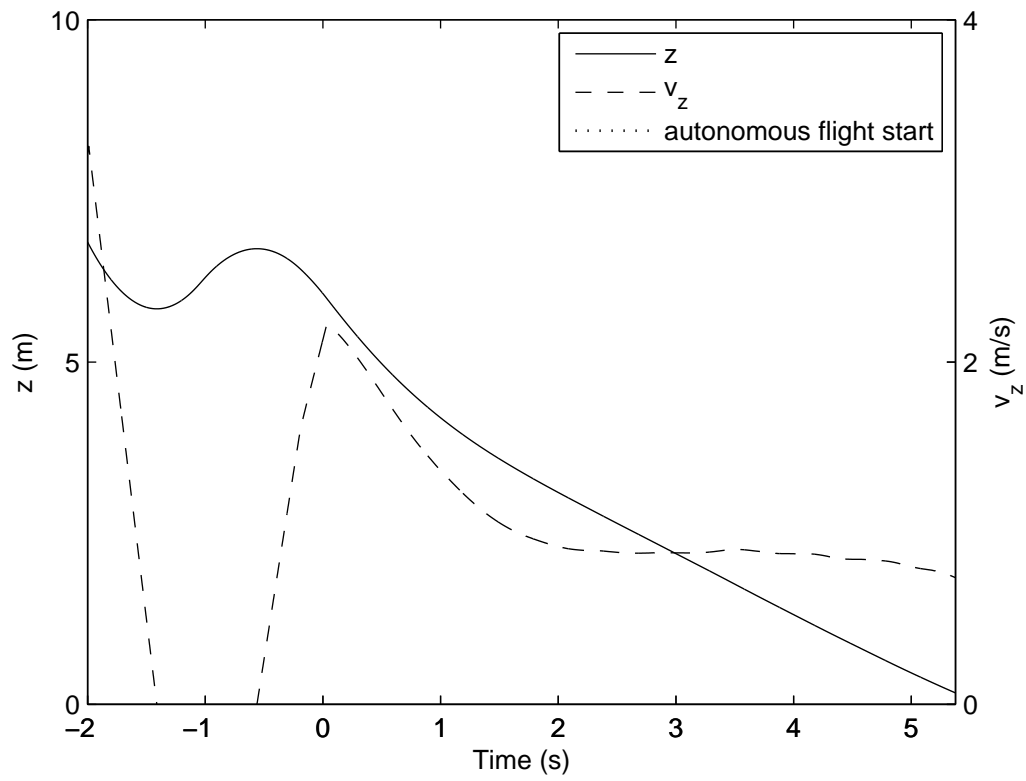

Fig. 15. Height (solid) and vertical velocity (dashed) obtained by simulation of the quadrotor performing autonomous landing with $k = 0.85$

The other reason behind the small velocity residual at touch down is the slow response of the control system dynamics to the large deviation from the visual reference near the ground. As the camera approaches the ground, the amount of image dilation increases exponentially and becomes very large even with the slightest motion near the ground, despite the fact that the same motion can produce a much smaller dilation magnitude when performed 3 meters above the ground. For this reason, the sensible choice for the control system designer would be accepting a slower tracking performance and some steady state errors of the visual tracking near the ground in exchange for more reliable and oscillation free operation near the ground. It should be pointed out that the Tau strategy has a major advantage over the constant image dilation approach with regard to this point for performing gap closure tasks. This is because the Tau strategy demands a linearly increasing amount of image dilation over time when landing, in contrast to a constant amount during the whole maneuver for the latter strategy. This would make the reference produced by the Tau strategy closer to the observed signal, and this relaxes the demands on the control system at this particular region. Using similar logic, the authors in [25] have chosen to adapt their landing strategy to produce an exponentially increasing image dilation reference to achieve landing with optimal fuel consumption. Why does nature chooses to adopt a linearly increasing image dilation (as in Tau strategy) while mass/acceleration optimality requires an exponentially increasing image dilation is still an open, and interesting, question.

Secondly, a slight oscillation in the estimated velocity can be observed in most experiments. This is due to two factors; the control system dynamics and the filtering and differentiation of the noisy ultrasonic height estimates. Note, however, that the vertical velocity signal shown in the figures is for monitoring purposes only and not used by the control system.

Now, to compare the achieved experimental results against the theoretical results it is important to isolate the effects of the initial conditions when the maneuver has been engaged. Hence, for comparison purposes, it is preferable to normalize height, the vertical velocity and the maneuver execution time, which only leaves the effects of the chosen maneuver constant to compare whether it affects the closure dynamics in accordance with theoretical expectations. Data shown in Figures 7 and 8 have been normalized and shown in Figures 16 and 17, respectively, where time has been normalized with the quantity $-\frac{\tau_0}{k}$ reflecting the maneuver execution time defined by (18).
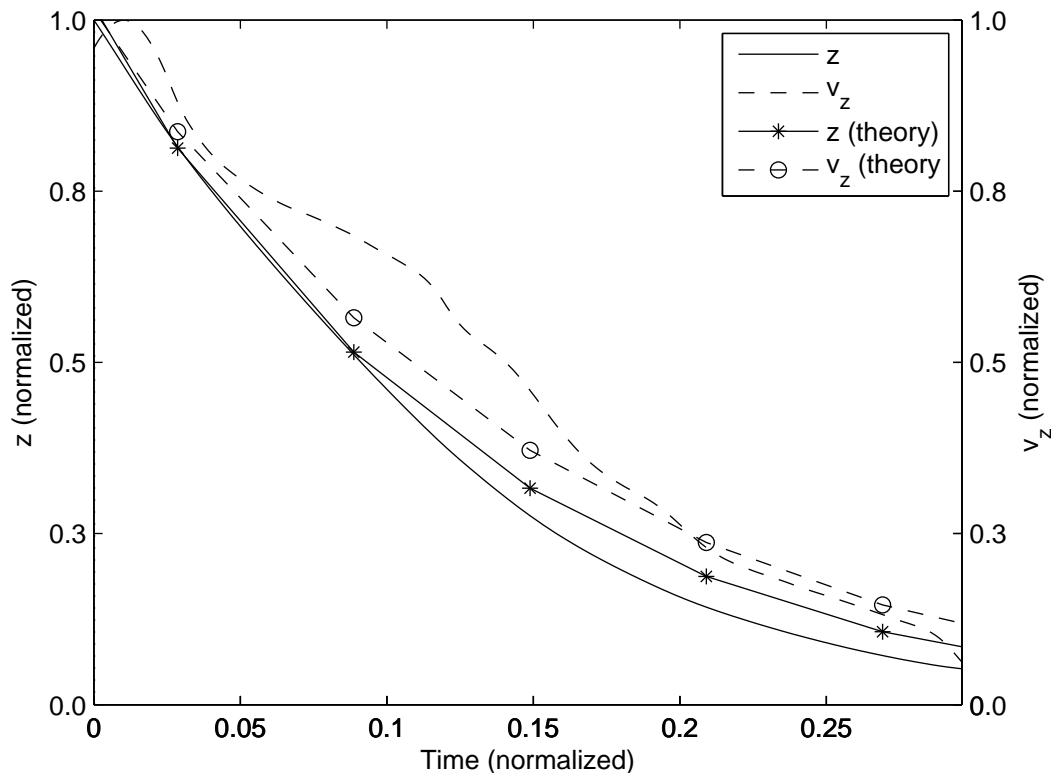

Fig. 16. Normalized height and vertical velocity against normalized time for quadrotor performing autonomous landing with k = 0.2. Theoretical values are superimposed

Comparing the landing velocity profile of both experiments 1 and 2 in the normalized plots in Figures 16 and 17 against the superimposed theoretical expected values shows a good correlation. The first experiment shows a more curved descent velocity profile as compared to the more linear velocity profile of the second experiment,
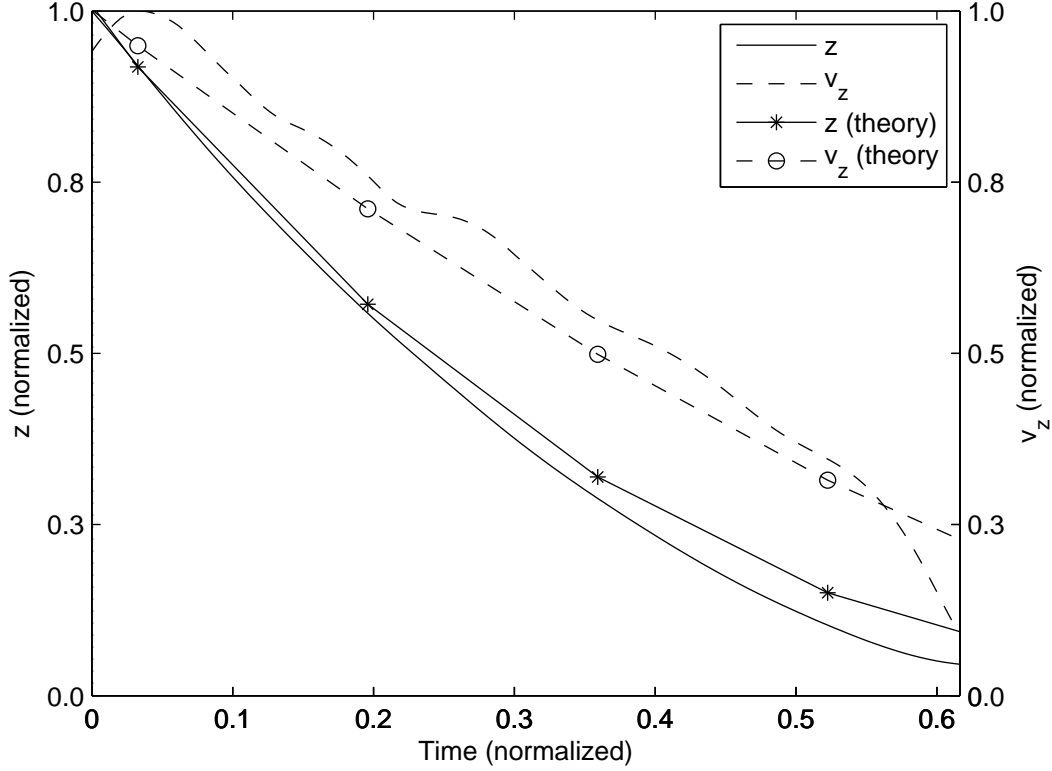
Fig. 17. Normalized height and vertical velocity against normalized time for quadrotor performing autonomous landing with k = 0.45. Theoretical values are superimposed

as expected. On the other hand, both maneuvers ended earlier than the expected execution time. This is again a result of the combined effects of the ground elevation of the camera in addition to the control system dynamics as discussed earlier. So, a small deviation from the expected theoretical closure dynamics is expected. However, this deviation is consistent across different runs and different maneuver constants, and hence the theoretical maneuver dynamics are preserved to some extent.

In support of the last argument, Figures 16 and 17, which are also normalized, show that the first experiment with $k = 0.2$ ended at about 30% of the theoretical maneuver execution time defined in (18), while the second experiment with $k = 0.45$ ended at about 65% of the theoretical maneuver execution time. The difference in the finish times of maneuvers with different values of k is expected, and is a result of choosing a different maneuver constant k, and can be verified by comparing the values of height z at the same points in time for different values of k in Figure 1. However, finishing the maneuvers 30% and 65% of the theoretical execution time have been found consistently in all the experiments performed with $k = 0.2$ and $k = 0.45$ respectively, including the experiments presented in this paper. The average normalized effective execution time ($t_{nef}(k)$) and its standard deviation σ are $t_{nef} = 0.3$ ($\sigma = 0.025$) for $k = 0.2$, and $t_{nef} = 0.63$ ($\sigma = 0.04$) for $k = 0.45$.

In addition to showing consistency with regard to effective execution time using the same maneuver constant, these results show consistency in the effective maneuver execution time across different maneuver constants as well. It can be seen from Figure 1 that the normalized height $z_n(k,t) = z(k,t)/z_0$ have similar values when evaluated at $t = t_{nef}(k)$ for $k = 0.2$ and $k = 0.45$. These normalized heights are found from (3) after normalization (as explained in Section II) and are evaluated to $z_n(0.2, 0.3) = 0.16$ and $z_n(0.45, 0.63) = 0.12$. This suggests that the control system as well as the camera elevation from the ground have introduced a combined effect causing the maneuvers to terminate when the normalized height z_n reaches an average value of $z_{nef} = 0.14$. The consistency of normalized effective final height z_{nef} values across different values of k is experimentally validated from the consistency of the normalized execution times $t_{nef}(k)$ values as shown above for $k = 0.2$ and $k = 0.45$, respectively.

Approximating the combined effects of the control system and the camera ground elevation by virtually raising the ground by a value of z_{nef} has two advantages. Firstly, the closure dynamics are preserved across different choices of k when the ground is virtually lifted, which makes the choice of different closure dynamics feasible in practice. Secondly, the effective landing time $t_{ef}(k)$ can be approximately determined from the choice of the

maneuver constant k due to the consistency of the values of $t_{nef}(k)$ experimentally found for different values of k. In order to find the value of the effective maneuver execution time $t_{ef}(k)$, the normalized effective final height z_{nef} as well as the normalized effective execution time $t_{nef}(k)$ are found empirically as explained in the previous paragraph. Then it can be deduced that the effective maneuver execution time $t_{ef}(k)$ is given by:

$$t_{ef}(k) = -t_{nef}(k)\frac{\tau_0}{k} \tag{42}$$

Equation (42) is used to find the ratio of the experimental maneuver execution time to the estimated finish time $t_{ef}(k)$ for the experiments performed with $k = 0.2$ and $k = 0.45$. The average ratio is found to be very close to unity (1.004 and 0.996 for each set, respectively) and the corresponding standard deviation is evaluated to 0.08 and 0.06 for each set, respectively. These numbers support the assumption that the effects of the practical implementation on the theoretical closure dynamics are consistent across different runs and different maneuver constants, so that it can be empirically accounted for. This finding facilitates the practical use of the proposed scheme not only for selecting desired closure dynamics, but also the approximate maneuver execution time.

When it comes to experiments that start from hover or with an upward velocity (experiments 3 and 4, respectively) the theoretical results become invalid, and hence are not useful for comparison. However, as the maneuver is still controlled with the same visual guidance law and the deviation is in the initial conditions, then it is expected that the feedback control system will compensate for the initial conditions. This suggests that in these cases the first part of the profile can be seen as a "catch up" portion while the second part should follow the theoretical results. This can be validated by noting that both experiments 3 and 4 shown in Figures 11 and 12, respectively, follow roughly the expected almost linear profile of maneuvers performed with $k = 0.45$ after 2.5 seconds following the maneuver initiation. Additionally, these experiments have been found to end at about 65% of the theoretical maneuver execution time, similarly to the previous experiments. Therefore, the deviation from the theoretical initial conditions can be tolerated in the first part of the maneuver, while the closure dynamics observed in the later part, which is probably the most important part of the maneuver, are more inline with the theoretically expected closure dynamics.

Finally, both ground approach maneuvers obtained with $k = -10$ and $k = -1.5$, shown in Figures 13 and 14, respectively, perform as expected. Although the maneuver execution time in ground approach mode is always valid, contrary to maneuvers with $k > 0$, the maneuver does nothing after the demanded image dilation approaches zero with speed proportional to the commanded $\dot{\tau}$ value. The initial rapid descent noticed at the start of the maneuver engagement is due to the demanded visual image dilation which quickly and exponentially decays with time, resulting in an altitude hold behavior after about 5 and 12 seconds for the first and second experiments, respectively. The first experiment runs shorter due to the smaller maneuver constant as expected. The altitude reductions due to the maneuvers were 0.7 and 1.3 meters, respectively, with a shorter drop in the first experiment as expected.

VIII. Conclusion

This paper has shown that the bio-inspired Tau strategy can be used to achieve flexible visual autonomous vertical control of Vertical Take-off and Landing (VTOL) vehicles. The practical experiments described in this paper have confirmed that near ground maneuvers, such as hovering, ground approach, and landing, can be visually performed without knowledge of the vehicle's height or vertical velocity. In addition, theoretical and experimental analysis of the maneuver parameters provided a method to practically control the task dynamics and its execution time. For the practical implementation of the strategy, the use of the integral form of the Tau strategy was necessary to avoid the issues associated with controlling a differentiated noisy signal. The use of the proposed visual dynamic filtering scheme, which was based on the unscented Kalman filter, helped to make possible the visual control results that were obtained.

Although there is no biological evidence to support the ground approach extension of the Tau theory proposed in this paper, it is possible to use this extension in practice as a simple method to approach the ground until further action is taken. Practical applications of such a maneuver include approaching the surface of a landing site or a docking station for inspection, then taking the landing or abort decision based on the outcome of the inspection. In principle, the same behavior can be achieved with a varying image dilation reference; however, the proposed ground approach method has the advantage of exploiting the same strategy already used for the other vertical maneuvers, leading to a simpler software implementation of the visual navigation sub-system.

Practical applications of the proposed method include not only VTOL vehicles, but also spacecraft landing and docking, as well as terrestrial navigation. Future work is required to automate the choice of critical maneuver parameters based on an understanding of the vehicle's objectives and context awareness.

APPENDIX

High-level PI controller parameters:

$$K_{P1} = 0.375$$
$$K_{I1} = 0.188$$
$$K_{P2} = 0.375$$
$$K_{I2} = 0.188 \tag{43}$$
$$K_{P3} = 2.788$$
$$K_{I3} = 0.067$$

Process noise covariance matrix used by the Unscented Kalman filter:

$$\boldsymbol{Q}_f = 10^{-5} \times \text{diag}(2.5, 2.5, 2.5, 2.5) \tag{44}$$

Low-level LQ tracker controller gain matrices:

$$\boldsymbol{K} = \begin{bmatrix} 0 & 530.3247 & -211.6108 & 0 & 42.3989 & -86.1182 \\ -529.9347 & 0 & 211.6108 & -40.0433 & 0 & 86.1182 \\ 0 & -530.3247 & -211.6108 & 0 & -42.3989 & -86.1182 \\ 529.9347 & 0 & 211.6108 & 40.0433 & 0 & 86.1182 \end{bmatrix} \tag{45}$$

$$\boldsymbol{F} = \begin{bmatrix} -211.6108 & -54.0872 & 0 & -21.525 \\ 211.6108 & 0 & -54.0474 & -21.525 \\ -211.6108 & 54.0872 & 0 & -21.525 \\ 211.6108 & 0 & 54.0474 & -21.525 \end{bmatrix} \tag{46}$$

REFERENCES

[1] S Saripalli, J F Montgomery, and G S Sukhatme. Visually guided landing of an unmanned aerial vehicle. *IEEE Transactions on Robotics and Automation*, 19(3):371–380, 2003.

[2] Bagen Wulan, Hu Jizhong, and Xu Yuanming. A Vision-Based Unmanned Helicopter Ship Board Landing System. In *Image and Signal Processing, 2009. CISP '09. 2nd International Congress on*, pages 1–5, 2009.

[3] O Shakernia, R Vidal, C S Sharp, Y Ma, and S Sastry. Multiple view motion estimation and control for landing an unmanned aerial vehicle. In *Robotics and Automation, 2002. Proceedings. ICRA '02. IEEE International Conference on*, volume 3, pages 2793–2798, 2002.

[4] M Meingast, C Geyer, and S Sastry. Vision based terrain recovery for landing unmanned aerial vehicles. In *Decision and Control, 2004. CDC. 43rd IEEE Conference on*, volume 2, pages 1670–1675 Vol.2, 2004.

[5] Yuan Zhengpeng, Gong Zhenbang, Wu Jiaqi, Chen Jinbo, and Rao Jinjun. A real-time vision-based guided method for autonomous landing of a rotor-craft unmanned aerial vehicle. In *Mechatronics and Automation, 2005 IEEE International Conference*, volume 4, pages 2212–2215 Vol. 4, 2005.

[6] Srikanth Saripalli. Vision-based autonomous landing of an helicopter on a moving target. AIAA Papaer 2009-5660, 2009.

[7] KarlEngelbert Engelbert Wenzel, Andreas Masselli, and Andreas Zell. Automatic Take Off, Tracking and Landing of a Miniature UAV on a Moving Carrier Vehicle. *Journal of Intelligent & Robotic Systems*, 61(1-4):221–238, October 2011.

[8] Dario Izzo and Guido de Croon. Nonlinear model predictive control applied to vision-based spacecraft landing. In *EURO GNC 2013, 2nd CEAS Specialist Conference on Guidance, Navigation & Control*, 2013.

[9] M D Tandale, R Bowers, and J Valasek. Trajectory tracking controller for vision-based probe and drogue autonomous aerial refueling. *Journal of Guidance Control and Dynamics*, 29(4):846, 2006.

[10] M Srinivasan, S Zhang, M Lehrer, and T Collett. Honeybee navigation en route to the goal: visual flight control and odometry. *Journal of Experimental Biology*, 199(1):237–244, 1996.

[11] N Franceschini, F Ruffier, and J Serres. *Optic flow based autopilots: speed control and obstacle avoidance*. 2009.

[12] D Izzo, N Weiss, and T Seidl. Constant-Optic-Flow Lunar Landing: Optimality and Guidance. *Journal of Guidance Control and Dynamics*, 34(5):1383, 2011.

[13] Herisse, X, B., T Hamel, R Mahony, and F X Russotto. Landing a VTOL Unmanned Aerial Vehicle on a Moving Platform Using Optical Flow. *IEEE Transactions on Robotics*, 28(1):77–89, 2012.

[14] R H Rasshofer and K Gresser. Automotive Radar and Lidar Systems for Next Generation Driver Assistance Functions. *Adv. Radio Sci.*, 3:205–209, May 2005.

[15] Franck Ruffier and Nicolas Franceschini. Optic flow regulation: the key to aircraft automatic guidance. *Robotics and Autonomous Systems*, 50(4):177–194, March 2005.

[16] D Honegger, L Meier, P Tanskanen, and M Pollefeys. An open source and open hardware embedded metric optical flow CMOS camera for indoor and outdoor applications. In *Robotics and Automation (ICRA), 2013 IEEE International Conference on*, pages 1736–1741, 2013.

[17] D N Lee. A theory of visual control of braking based on information about time-to-collision. *Perception*, 5(4):437–459, 1976.

[18] R T Spurr. Subjective aspects of braking. *Automobile Engineer*, 1969.

[19] David N Lee and Paul E Reddish. Plummeting gannets: a paradigm of ecological optics. *Nature*, 293(5830):293–294, 1981.

[20] David N Lee, David S Young, and Dennis Rewt. How do somersaulters land on their feet? *Journal of Experimental Psychology: Human Perception and Performance*, 18(4):1195–1202, 1992.

[21] D N Lee, M N O Davies, and P R Green. Visual control of velocity of approach by pigeons when landing. *Journal of Experimental Biology*, 180(1):85–104, 1993.

[22] D N Lee, P E Reddish, and D T Rand. Aerial docking by hummingbirds. *Naturwissenschaften*, 78(11):526–527, 1991.

[23] Y Shimada, R Seto, and K Ito. Detection of the tau-margin and application to autonomous control of a flying robot. In *Intelligent Sensors, Sensor Networks and Information Processing (ISSNIP), 2009 5th International Conference on*, pages 103–108, 2009.

[24] Y Miyagawa, Y Kondo, and K Ito. Realization of flock behavior by using tau-margin. In *Control Automation and Systems (ICCAS), 2010 International Conference on*, pages 957–961, 2010.

[25] Dario Izzo and Guido De Croon. Landing with Time-to-Contact and Ventral Optic Flow Estimates. *Journal of Guidance, Control, and Dynamics*, 35(4):1362–1367, July 2012.

[26] Pu Xie, Ou Ma, and Zhen Zhang. A Bio-inspired Approach for UAV Landing and Perching. AIAA Papaer 2013-5108, 2013.

[27] Farid Kendoul. Four-dimensional guidance and control of movement using time-to-contact: Application to automated docking and landing of unmanned rotorcraft systems. *The International Journal of Robotics Research*, 33(2):237–267, February 2014.

[28] Roland Brockers, Sara Susca, David Zhu, and Larry Matthies. Fully self-contained vision-aided navigation and landing of a micro air vehicle independent from external sensor inputs. In *SPIE Defense, Security, and Sensing*, pages 83870Q–83870Q–10. International Society for Optics and Photonics, May 2012.

[29] Stephan Weiss, Markus W Achtelik, Simon Lynen, Michael C Achtelik, Laurent Kneip, Margarita Chli, and Roland Siegwart. Monocular Vision for Long-term Micro Aerial Vehicle State Estimation: A Compendium. *Journal of Field Robotics*, 30(5):803–831, 2013.

[30] T Bresciani. *Modelling, identification and control of a quadrotor helicopter*. Master thesis, Lund University, 2008.

[31] Brian L Stevens and Frank L Lewis. *Aircraft control and simulation*, page 27. Wiley New York, 2 edition, 2003.

[32] J H Wang. An Active Low-Order Fault-Tolerant State Space Self-Tuner for the Unknown Sample-Data Linear Regular System with an Input-Output Direct Feedthrough Term. *Applied mathematical sciences*, 6(97):4813, 2012.

[33] Dennis M Shaffer, Scott M Krauchunas, Marianna Eddy, and Michael K McBeath. How Dogs Navigate to Catch Frisbees. *Psychological Science*, 15(7):437–441, 2004.

[34] D M Shaffer and T B Gregory. How Football Players Determine where to Run to Tackle other Players: A Mathematical and Psychological Description and Analysis. *The Open Sports Sciences Journal*, 2:29–36, 2009.

[35] Mohamad T Alkowatly, Victor M Becerra, and William Holderbaum. Estimation of Visual Motion Parameters Used for Bio-inspired Navigation. *Journal of Image and Graphics*, 1(3):120–124, 2013.

[36] G C H E de Croon, H W Ho, C De Wagter, E Van Kampen, B Remes, and Q P Chu. Optic-flow based slope estimation for autonomous landing. *International Journal of Micro Air Vehicles*, 5(4):287–298, 2013.

[37] H C Longuet-Higgins and K Prazdny. The Interpretation of a Moving Retinal Image. *Proceedings of the Royal Society of London. Series B. Biological Sciences*, 208(1173):385–397, 1980.

[38] P H Menold and R K Pearson. Online outlier detection and removal. In *Proceedings of the 7th Mediterranean Conference on Control and Automation (MED99)*, pages 1110–1133, 1999.

[39] L R Harris, M R Jenkin, D Zikovitz, F Redlick, P Jaekl, U T Jasiobedzka, H L Jenkin, and R S Allison. Simulating Self-Motion I: Cues for the Perception of Motion. *Virtual Reality*, 6(2):75–85, 2002.

[40] Timothy C.Hain and Janet O.Helminski. Anatomy and physiology of the normal vestibular system. In *Vestibular Rehabilitation Contemporary perspectives in rehabilitation*, chapter 1. F.A. Davis Company, 2007.

[41] Simon J Julier and Jeffrey K Uhlmann. Unscented filtering and nonlinear estimation. *Proceedings of the IEEE*, 92(3):401–422, 2004.

[42] John L Crassidis and John L Junkins. *Optimal estimation of dynamic systems*, pages 196–198. CRC press, 2011.

[43] R Kandepu, L Imsland, and Bjarne A Foss. Constrained state estimation using the unscented kalman filter. In *Proceedings of the 16th Mediterranean Conference on Control and Automation*, pages 1453–1458, 2008.

[44] Lennart Ljung. *System identification: theory for the user*, chapter 7. Prentice-Hall, Upper Saddle River, NJ, USA, 2 edition, 1999.